Computationally Efficient Fixed Switching Frequency Direct Model Predictive Control

Qifan Yang, *Student Member, IEEE*, Petros Karamanakos, *Senior Member, IEEE*, Wei Tian, *Student Member, IEEE*, Xiaonan Gao, *Member, IEEE*, Xinyue Li, *Student Member, IEEE*, Tobias Geyer, *Senior Member, IEEE*, and Ralph Kennel, *Senior Member, IEEE*

***Abstract*—This paper presents a direct model predictive control (MPC) method for drive systems with superior steady-state and dynamic performance. Specifically, the discussed MPC algorithm achieves a steady-state behavior that is similar or better than that of a linear controller with a dedicated modulator, and fast transient responses that characterize direct controllers. Moreover, it ensures a fixed switching frequency by allowing for one switching transition per phase and sampling interval. Furthermore, the controller utilizes the stator current gradient to predict the evolution of the drive system within the prediction horizon. To find the optimal switching time instants—and thus ensure favorable performance—the control and modulation problems are formulated in one computational stage as a constrained quadratic program (QP). To solve the latter within a few microseconds, a computationally efficient QP solver based on a gradient method is proposed that enables the real-time implementation of the presented algorithm. To further alleviate the computational demands of the proposed method, a mechanism that can identify suboptimal switching sequences at the very early stages of the optimization process is proposed. The effectiveness of the proposed control scheme is experimentally verified on a 3 kW drive system consisting of a two-level inverter and an induction machine.**

***Index Terms*—AC drives, model predictive control (MPC), direct control, quadratic programming, power electronic systems.**

I. Introduction

FINITE control set model predictive control (FCS-MPC) is a control method for power electronics that has gained popularity in the last decade [1], [2]. A direct control strategy, FCS-MPC exploits the discrete nature of power converters by considering the control inputs from a finite set for which the future behavior of the power electronic system is predicted. To compute the optimal control input, i.e., the converter switch position, that results in the most desirable system behavior, as quantified by a performance criterion (or criteria), the output reference tracking and modulation problems are formulated in one computational stage [3]. This control scheme can achieve fast transient responses, but also suffers from several drawbacks, such as variable switching frequency and spread harmonic spectra with increased harmonic energy, especially when poorly designed [4]. When electric drives are of interest, such harmonic current distortions can lead to increased iron and copper losses [5].

Considering the above-mentioned drawbacks of FCS-MPC, some methods have been presented that aim to address them. For example, a frequency-weighted MPC scheme was proposed in [6], where a band-stop filter was included in the controller so that the underlying optimization problem accounted for the current spectral properties. However, even though the current harmonic spectra can be shaped to some extent, the switching frequency cannot be made constant. In [7] and [8], direct MPC schemes were combined with a separate modulator to ensure a constant converter switching frequency. By doing so, however, the inherent fast dynamics of direct control schemes are compromised due to the presence of a modulator. Other works, such as [9]–[17], propose direct MPC algorithms with an implicit modulator, i.e., the switch position is not limited to change only at the discrete time instants—as with conventional FCS-MPC—but it can change at any time instant within the sampling interval. Such MPC schemes compute not only the optimal switch positions, but also the associated time instants within the sampling interval they have to be applied to the converter, such that the ripples of the controlled variables, e.g., stator current, electromagnetic torque, stator flux magnitude, etc., are reduced. However, methods such as [11]–[14], [16]–[18] do not guarantee global optimality, whereas the algorithms in [10], [15] do not ensure a fixed switching frequency. Moreover, it is worth mentioning that the techniques in [9], [12], [14], [17], [18], while operating the converter at a constant switching frequency, produce nondiscrete harmonic spectra due to the fact that the computed switching patterns are not repetitive.

An alternative approach to tackle both problems of variable switching frequency and nondiscrete harmonic spectra in direct MPC schemes is to use the so-called pre-computed switching sequences [19]–[22]. These control schemes compute the optimal switching time of specific switching sequences. To this aim, the optimization problem is formulated as an *unconstrained* quadratic program (QP) which allows for an analytical solution. As a result, the computational complexity of the MPC problem is greatly reduced, thus addressing the inherent disadvantage of FCS-MPC that relates to its high computational requirements [4]. Nevertheless, due to the unconstrained nature of the optimization problem, such methods

Q. Yang, W. Tian, X. Gao and R. Kennel are with the Chair of Electrical Drive Systems and Power Electronics, Technical University of Munich, 80333 Munich, Germany; e-mail: qifan.yang@tum.de, wei.tian@tum.de, xiaonan.gao@tum.de, raphel.kennel@tum.de

P. Karamanakos is with the Faculty of Information Technology and Communication Sciences, Tampere University, 33101 Tampere, Finland; e-mail: p.karamanakos@ieee.org

X. Li is with Bosch Rexroth AG, 97816 Lohr am Main, Germany; e-mail: xinyue.li@boschrexroth.de

T. Geyer is with ABB Systems Drives, 5300 Turgi, Switzerland; e-mail: t.geyer@ieee.org

do not always guarantee optimality or symmetrical switching sequences, and thus discrete harmonic spectra. Moreover, although [23] imposes constraints on the applications times, it is limited to simple single-output systems, such as dc-dc converters.

Motivated by the shortcomings of the aforementioned MPC algorithms and the associated challenges, [24] presented a direct MPC method with a fixed switching frequency for variable speed drive systems. This control technique manages to both minimize the stator current distortions and operate the drive at the desired (constant) switching frequency. The former is fulfilled by capturing an approximate value of the rms current ripple in the objective function. To achieve the latter, [24] ensures that each of the three converter phase legs switches within the sampling interval in a specific chronological order and only once, introducing, in essence, a fixed modulation half-cycle, similar to carrier-based pulsewidth modulation (CB-PWM) or space vector modulation (SVM) [25]. In doing so, repetitive, symmetrical switching sequences are applied to the converter, which result in discrete stator current harmonic spectra, with harmonic energy located only at odd nontriplen multiples of the fundamental frequency. Moreover, given that the optimization problem underlying direct MPC is formulated as a *constrained* QP, optimality is guaranteed, thus the best possible behavior of the drive is ensured for the whole range of operating conditions. To achieve this, nevertheless, [24] has to solve six constrained QPs (one for each possible switching sequence) in real time before concluding to the global optimal solution, i.e., the optimal sequence of switch positions and the corresponding switching time instants. Consequently, the associated computational burden hindered the real-time implementation, and thus experimental validation, of the method.

To significantly reduce the computational complexity of the direct MPC method in [24], this paper presents a computationally efficient solution of the underlying MPC problem, thus rendering its real-time implementation possible. To this end, this paper tackles the challenges of the real-time implementation, which are twofold. First, although several open-source and commercial QP solvers are available [2, Section IV], they are commonly designed for general QP problems. Consequently, they may not be able to solve the MPC problem of interest in real time within a few hundred, or even tens, of microseconds, since they do not exploit its structure. Indeed, the execution time greatly depends on various factors of the optimization problem, such as the size of the state and input vectors, the number of the constraints and the geometry of the feasible region, see [26] for a comprehensive assessment of different QP solvers. Therefore, to facilitate the real-time implementation of the direct MPC algorithm, an efficient and highly reliable gradient-based QP solver is developed in this paper. This algorithm exploits the properties of the QP problem at hand and achieves a fast and reliable convergence.

To further reduce the computational demands of the MPC algorithm, a method is introduced to deal with the second challenge of the real-time implementation, namely the need to solve a unique constrained QP for each one of the six possible switching sequences within each sampling interval. Since not all switching sequences are good candidate solutions at any given instant of the problem, the corresponding QPs may be ill-posed, leading to poor convergence rates and thus longer solving times. To tackle this issue, a mechanism is proposed that can detect the unsuited switching sequences with only a few computations. Thanks to this, only one or two QPs need to be solved at each sampling interval, while still guaranteeing global optimality. As a result, the direct MPC scheme becomes computationally tractable, without sacrificing its performance. To show this, the controller is experimentally evaluated with a drive system consisting of a three-phase two-level voltage source inverter and an induction machine (IM).

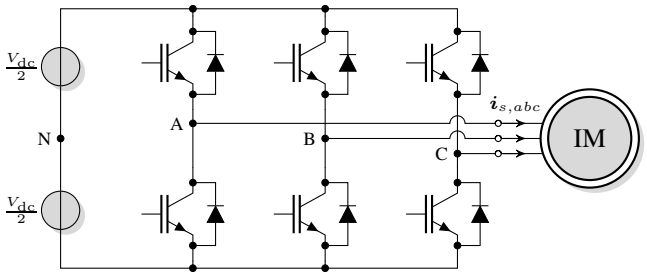

Fig. 1: Two-level three-phase voltage source inverter driving an IM.

This paper is structured as follows. Section II introduces the mathematical model of the case study of this paper. The direct MPC scheme is presented in Section III. In Section IV, the proposed gradient-based QP algorithm is explained along with the detection mechanism of the unsuited switching sequences. The performance of the proposed control scheme is experimentally evaluated in Section V. Finally, conclusions are drawn in Section VI.

II. Mathematical Model Of The System

The examined system consists of a three-phase two-level voltage source inverter and an IM, as shown in Fig. 1. The dc-link voltage is assumed to be constant and equal to its nominal value $V_{\rm dc}$. The modeling of the system as well as the formulation of the control problem are done in the stationary orthogonal $\alpha\beta$ reference frame. Therefore, the Clarke transformation matrix

$$\boldsymbol{K} = \frac{2}{3}\begin{bmatrix} 1 & -\frac{1}{2} & -\frac{1}{2} \\ 0 & \frac{\sqrt{3}}{2} & \frac{\sqrt{3}}{2} \end{bmatrix} \tag{1}$$

is employed to map a variable $\boldsymbol{\xi}_{abc} = [\xi_a \ \xi_b \ \xi_c]^T$ in the abc-plane into a variable $\boldsymbol{\xi}_{\alpha\beta} = [\xi_\alpha \ \xi_\beta]^T$ in the $\alpha\beta$-plane.[1]

Let $\boldsymbol{u}_{abc} = [u_a \ u_b \ u_c]^T$ denote the three-phase switch position of the two-level inverter, where $u_x \in \mathcal{U} = \{-1, 1\}$, with $x \in \{a, b, c\}$, is the single-phase switch position. In each phase, the values -1 and 1 correspond to the phase voltages $-\frac{V_{\rm dc}}{2}$ and $\frac{V_{\rm dc}}{2}$, respectively. Thus, the voltage applied to the machine terminals $\boldsymbol{v}_s$ is

$$\boldsymbol{v}_s = \frac{V_{\rm dc}}{2}\boldsymbol{u} = \frac{V_{\rm dc}}{2}\boldsymbol{K}\boldsymbol{u}_{abc}\,. \tag{2}$$

The dynamics of the squirrel-cage IM can be fully described by the differential equations that involve the stator current $\boldsymbol{i}_s$,

[1] In the sequel of the paper, the subscript $\alpha\beta$ used to denote variables in the $\alpha\beta$-plane is omitted to simplify the notation.

the rotor flux $\boldsymbol{\psi}_r$, and the angular speed of the rotor ω_r. This leads to [27]

$$\frac{\mathrm{d}\boldsymbol{i}_s}{\mathrm{d}t} = -\frac{1}{\tau_s}\boldsymbol{i}_s + \left(\frac{1}{\tau_r}\boldsymbol{I}_2 - \omega_r \begin{bmatrix} 0 & -1 \\ 1 & 0 \end{bmatrix}\right)\frac{X_m}{D}\boldsymbol{\psi}_r + \frac{X_r}{D}\boldsymbol{v}_s \tag{3a}$$

$$\frac{\mathrm{d}\boldsymbol{\psi_r}}{\mathrm{d}t} = \frac{X_m}{\tau_r}\boldsymbol{i}_s - \frac{1}{\tau_r}\boldsymbol{\psi}_r + \omega_r \begin{bmatrix} 0 & -1 \\ 1 & 0 \end{bmatrix}\boldsymbol{\psi}_r \tag{3b}$$

$$\frac{\mathrm{d}\omega_r}{\mathrm{d}t} = \frac{1}{\Theta}(T_e - T_\ell)\,, \tag{3c}$$

where R_s (R_r) is the stator (rotor) resistance, X_{ls} (X_{rs}) the stator (rotor) leakage reactance, and X_m the mutual reactance. Moreover, $\tau_s = X_r D/(R_s X_r^2 + R_r X_m^2)$ and $\tau_r = X_r/R_r$ are the transient stator and rotor time constants, respectively, where the constant D is defined as $D = X_s X_r - X_m^2$, with $X_s = X_{ls} + X_m$ and $X_r = X_{lr} + X_m$. Finally, Θ is the moment of inertia, while T_e and T_ℓ are the electromagnetic and load torque, respectively.

Based on (2) and (3), the model of the drive system in continuous-time state-space representation is written as

$$\frac{\mathrm{d}\boldsymbol{x}(t)}{\mathrm{d}t} = \boldsymbol{F}\boldsymbol{x}(t) + \boldsymbol{G}\boldsymbol{K}\boldsymbol{u}_{abc}(t) \tag{4a}$$

$$\boldsymbol{y}(t) = \boldsymbol{C}\boldsymbol{x}(t)\,, \tag{4b}$$

where the state vector is $\boldsymbol{x} = [i_{s\alpha}\ i_{s\beta}\ \psi_{r\alpha}\ \psi_{r\beta}]^T$,[2] while the three-phase switch position and the stator current are the system input and output, respectively, i.e., $\boldsymbol{u}_{abc} = [u_a\ u_b\ u_c]^T$ and $\boldsymbol{y} = [i_{s\alpha}\ i_{s\beta}]^T$. Moreover, matrices $\boldsymbol{F}$, $\boldsymbol{G}$, and $\boldsymbol{C}$ are the system, input and output matrices, respectively, and they can be easily derived from (3) [3, Appendix 5.A].

Finally, by using forward Euler discretization the discrete-time state-space model of the system is derived as

$$\boldsymbol{x}(k+1) = \boldsymbol{A}\boldsymbol{x}(k) + \boldsymbol{B}\boldsymbol{K}\boldsymbol{u}_{abc}(k) \tag{5a}$$

$$\boldsymbol{y}(k) = \boldsymbol{C}\boldsymbol{x}(k)\,, \tag{5b}$$

with $k \in \mathbb{N}$, $\boldsymbol{A} = \boldsymbol{I} + \boldsymbol{F}T_s$, and $\boldsymbol{B} = \boldsymbol{G}T_s$, where $\boldsymbol{I}$ is the identity matrix of appropriate dimensions, and T_s the sampling interval.

III. Direct MPC with Fixed Switching Frequency

The discussed MPC algorithm was initially proposed in [24] and refined in [28]. In the sequel of this section, the main principles and characteristics of the controller are presented.

A. Control Problem

The main objective of the controller is to minimize the stator current ripple and keep the switching frequency of the converter constant. To do so, each phase of the converter is allowed to switch once within the sampling intervals T_s, as exemplified in Fig. 2(a).

Let t_i, $i \in \{1, 2, 3\}$, denote the switching instants that are placed in an ascending order within one sampling interval

[2]Note that due to the slower mechanical dynamics, the angular speed of the rotor ω_r is treated as a (relatively slowly) varying parameter rather than as a state variable.

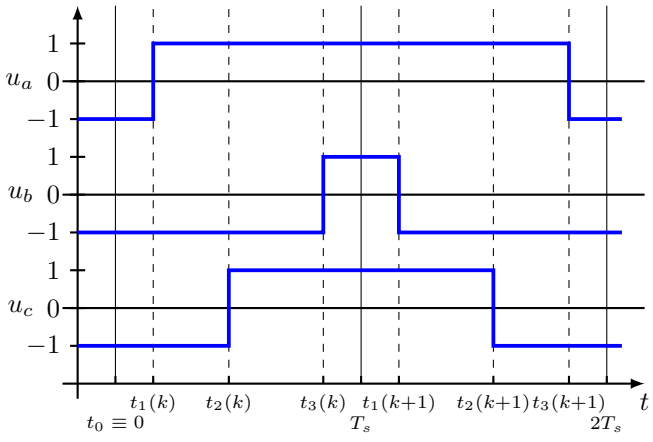

(a) Three-phase switch position.

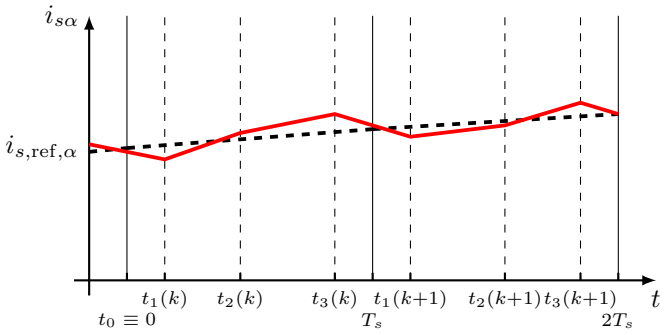

(b) Stator current (α-component).

Fig. 2: Example of the evolution of $i_{s\alpha}$ over two sampling intervals by applying the depicted switching sequence.

T_s, i.e., $0 \le t_1 \le t_2 \le t_3 \le T_s$. Thus, each sampling interval is divided into four sub-intervals $[0, t_1)$, $[t_1, t_2)$, $[t_2, t_3)$ and $[t_3, T_s)$, which are the application times of four switch positions. Specifically, at the beginning of the current sampling $t_0 \equiv 0$, and until t_1, the last switch position applied in the previous T_s is applied, i.e., $\boldsymbol{u}_{abc}(t_0) = \boldsymbol{u}_{abc}(t_0^-)$. At time instant t_1, a switching transition is performed in one of the three phases, implying that the switch position $\boldsymbol{u}_{abc}(t_1)$ is applied. Following, at time instant t_2, the switch position $\boldsymbol{u}_{abc}(t_2)$ is applied such that one of the two thus far inactive phases is switched. Finally, the only inactive phase left is forced to switch at time instant t_3 by applying switch position $\boldsymbol{u}_{abc}(t_3)$. As can be understood, by following this principle, the three phases of the system can switch in six possible combinations, see the left-hand side of Table I. For example, phase a may switch first, followed by consecutive changes in phases b and c, or vice versa, etc.

The above concept can be extended to longer prediction horizons, which are adopted in this work due to the improvements they bring in the steady-state performance [29]. However, as shown in [28], to keep the number of possible switching sequences constant and equal to six—instead of increasing it exponentially with the horizon steps N_p, i.e., 6^{N_p}—the switching sequences are mirrored with respect to the discrete time steps in a consecutive fashion, similar to, e.g., the SVM switching pattern [25]. Considering that a two-step horizon ($N_p = 2$) is implemented in this work, this means

TABLE I: Possible switching sequences for a two-step horizon.

Number of sequence	Phase with the switching transition					
	1^{st} sampling interval			2^{nd} sampling interval		
	First	Second	Third	First	Second	Third
1	a	b	c	c	b	a
2	a	c	b	b	c	a
3	b	a	c	c	a	b
4	b	c	a	a	c	b
5	c	a	b	b	a	c
6	c	b	a	a	b	c

that the switching sequence in the second prediction interval mirrors that of the first prediction interval with respect to T_s, as illustrated in Fig. 2(a). Table I summarizes all possible switching sequences over a two-step prediction.

To describe the above, the vector of switching time instants $\boldsymbol{t}$ and the vector of switch positions (i.e., the switching sequence) $\boldsymbol{U}$ are introduced. These are defined as

$$\boldsymbol{t} = \begin{bmatrix} \boldsymbol{t}^T(k) & \boldsymbol{t}^T(k+1) \end{bmatrix}^T \tag{6a}$$

$$\boldsymbol{U} = \begin{bmatrix} \boldsymbol{U}^T(k) & \boldsymbol{U}^T(k+1) \end{bmatrix}^T, \tag{6b}$$

where

$$\boldsymbol{t}(\ell) = \begin{bmatrix} t_1(\ell) & t_2(\ell) & t_3(\ell) \end{bmatrix}^T \tag{7a}$$

$$\boldsymbol{U}(\ell) = \begin{bmatrix} \boldsymbol{u}_{abc}^T(t_0(\ell)) & \boldsymbol{u}_{abc}^T(t_1(\ell)) & \boldsymbol{u}_{abc}^T(t_2(\ell)) & \boldsymbol{u}_{abc}^T(t_3(\ell)) \end{bmatrix}^T. \tag{7b}$$

with $\ell \in \{k, k+1\}$. It is important to point out that, as explained above, it is implied that $\boldsymbol{U}(k+1) = [\boldsymbol{u}_{abc}^T(t_3(k)) \;\; \boldsymbol{u}_{abc}^T(t_2(k)) \;\; \boldsymbol{u}_{abc}^T(t_1(k)) \;\; \boldsymbol{u}_{abc}^T(t_0(k))]^T$, i.e., $\boldsymbol{u}_{abc}(t_0(k+1)) = \boldsymbol{u}_{abc}(t_3(k))$, $\boldsymbol{u}_{abc}(t_1(k+1)) = \boldsymbol{u}_{abc}(t_2(k))$, $\boldsymbol{u}_{abc}(t_2(k+1)) = \boldsymbol{u}_{abc}(t_1(k))$, and $\boldsymbol{u}_{abc}(t_3(k+1)) = \boldsymbol{u}_{abc}(t_0(k))$. Note, however, that the switching times may be asymmetric, thus $t_1(k)$ is not necessarily equal to $2T_s - t_3(k+1)$, etc.

B. Control Method

The main control objective is the minimization of the (approximate) rms stator current error, since this corresponds to the minimization of the stator current total harmonic distortion (THD) [30, Appendix A]. As explained in [24] and [28], this goal can be mapped into the objective function

$$J = \sum_{\ell=k}^{k+1} \left(\sum_{i=1}^{3} \|\boldsymbol{i}_{s,\text{ref}}(t_i(\ell)) - \boldsymbol{i}_s(t_i(\ell))\|_2^2 + \left\|\boldsymbol{\Lambda}\big(\boldsymbol{i}_{s,\text{ref}}(T_s(\ell)) - \boldsymbol{i}_s(T_s(\ell))\big)\right\|_2^2 \right), \tag{8}$$

where the current tracking error is penalized at the switching instants and at the discrete time steps. Note that the diagonal, positive definite matrix $\boldsymbol{\Lambda} \succ 0 \in \mathbb{R}^{2\times 2}$ is introduced to penalize more heavily the tracking error at the discrete time steps. As explained in [28, Section III], by doing so, symmetry in the applied switching sequences is enforced, which enables the elimination of undesired low-frequency harmonics.

To find the optimal switching time instants $\boldsymbol{t}^*$, the current error, as quantified by (8), needs to be computed for all six possible switching sequences $\boldsymbol{U}$, as mentioned in Section III-A. To do so, the evolution of the stator current $\boldsymbol{i}_s$ within all the subintervals of the prediction horizon needs to be computed for each $\boldsymbol{U}$. Given that the sampling interval T_s is much smaller than the fundamental period T_1, i.e., $T_s \ll T_1$, it is assumed that the derivative of the stator current when applying a switching transition is constant within T_s. Such an assumption implies that the stator current trajectories within the subintervals of the horizon can be described by their corresponding gradients, i.e.,

$$\boldsymbol{m}(t_i(\ell)) = \frac{\mathrm{d}\boldsymbol{i}_s(t_i(\ell))}{\mathrm{d}t} = \boldsymbol{C}(\boldsymbol{F}\boldsymbol{x}(t_0(k)) + \boldsymbol{G}\boldsymbol{K}\boldsymbol{u}_{abc}(t_i(\ell)))\,, \tag{9}$$

where $i \in \{0,1,2,3\}$ and $\ell = k, k+1$. Note that because of the assumption of constant gradients within T_s, (9) computes the gradients at the switching instants $t_1(\ell)$, $t_2(\ell)$, and $t_3(\ell)$ based on the measured/estimated state, i.e., $\boldsymbol{x}(t_0(k))$.

Utilizing the gradients provided by (9), the stator current at the switching instants and discrete time steps can be calculated as

$$\boldsymbol{i}_s(t_i(\ell)) = \boldsymbol{i}_s(t_{i-1}(\ell)) + \boldsymbol{m}(t_{i-1}(\ell))(t_i(\ell) - t_{i-1}(\ell))\,, \tag{10}$$

with $i \in \{1,2,3,4\}$ and $t_4 = T_s$.

On the same principle, the current reference is assumed to evolve in a piecewise linear fashion within the horizon, with a constant gradient for each prediction step, given by

$$\boldsymbol{m}_{\text{ref}}(\ell) = \frac{\boldsymbol{i}_{s,\text{ref}}(\ell+1) - \boldsymbol{i}_{s,\text{ref}}(\ell)}{T_s}\,. \tag{11}$$

Hence, the current reference over the horizon is

$$\boldsymbol{i}_{s,\text{ref}}(t) = \boldsymbol{i}_{s,\text{ref}}(\ell) + \boldsymbol{m}_{\text{ref}}(\ell)\,t\,. \tag{12}$$

An example of the stator current evolution and the corresponding reference on the α-axis is shown in Fig. 2(b).

Finally, based on expressions (9) to (12), and after some algebraic manipulations, function (8) can be written in vector form as

$$J = \|\boldsymbol{r} - \boldsymbol{M}\boldsymbol{t}\|_2^2\,, \tag{13}$$

where the vector $\boldsymbol{r} \in \mathbb{R}^{8N_p}$ and matrix $\boldsymbol{M} \in \mathbb{R}^{8N_p \times 3N_p}$, with $N_p = 2$, are given in the appendix.

C. Control Algorithm

Taking into account the control principles developed in Sections III-A and III-B, the direct MPC algorithm is summarized in the following.

In a first step, the *seven* unique stator current gradients are computed based on the measured/estimated state vector $\boldsymbol{x}(t_0)$ and the possible *eight* switch positions $\boldsymbol{u}_{abc}$, i.e.,

$$\boldsymbol{m}_w = \boldsymbol{C}(\boldsymbol{F}\boldsymbol{x}(t_0) + \boldsymbol{G}\boldsymbol{u}_w)\,, \tag{14}$$

where $w \in \{0,1,\ldots,6\}$. Note that in (14), $\boldsymbol{u}_w = \boldsymbol{K}\boldsymbol{u}_{abc,w}$ stands for the unique voltage vectors in the $\alpha\beta$-plane (six active and one zero vector), see Fig. 3, where $\boldsymbol{u}_j$, $j \in \{1,2,\ldots,6\}$, are the active vectors, and $\boldsymbol{u}_0/\boldsymbol{u}_7$ the zero vector.

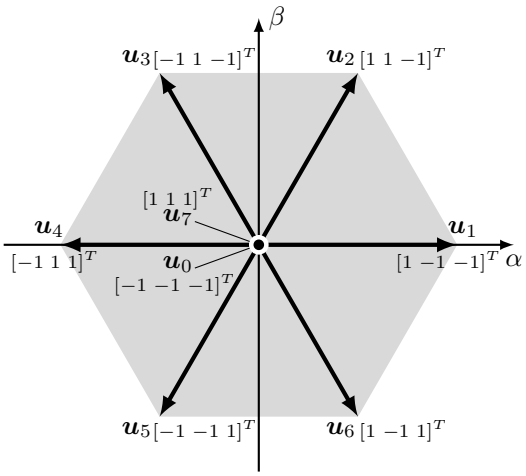

Fig. 3: Two-level inverter switch positions in the stationary ($\alpha\beta$) plane.

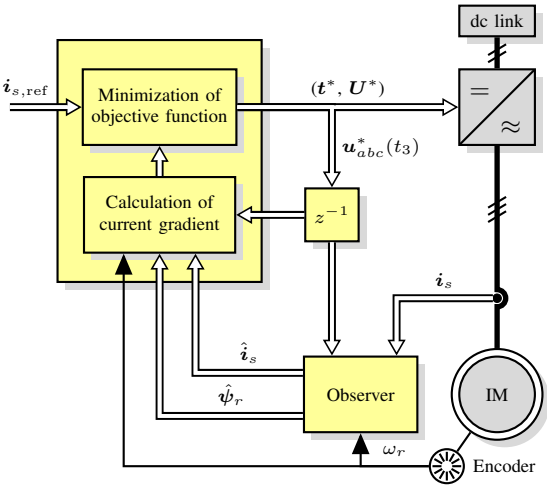

Fig. 4: Fixed switching frequency direct MPC for a two-level three-phase voltage source inverter driving an IM.

Subsequently, the controller enumerates the six possible switching sequences $\boldsymbol{U}_z$, $z \in \{1, 2, \ldots, 6\}$, shown in Table I. For each one of them, an optimization problem of the form

$$\begin{aligned} \underset{\boldsymbol{t} \in \mathbb{R}^6}{\text{minimize}} \quad & \|\boldsymbol{r} - \boldsymbol{M}\boldsymbol{t}\|_2^2 \\ \text{subject to} \quad & 0 \le t_1(k) \le t_2(k) \le t_3(k) \le T_s \\ & \le t_1(k+1) \le t_2(k+1) \le t_3(k+1) \le 2T_s \end{aligned} \tag{15}$$

is formulated. According to [24] and [28], the QP (15) has to be solved six times—once for each $\boldsymbol{U}_z$—based on an off-the-self QP solver [2, Section IV] to yield $\boldsymbol{t}_z$ and the associated cost J_z. However, in this work, (15) is efficiently solved by the QP solver proposed in Section IV. Moreover, as explained in that section, the developed solver can detect unsuited $\boldsymbol{U}_z$ with a simple one-step projection method, meaning that at most two QPs (15) need to be solved in real time. As a result, the computational burden of the direct MPC algorithm is kept modest, thus facilitating its real-time implementation.

In a last step, the pair of switching sequence and time instants that is globally optimal, i.e., $\{\boldsymbol{U}^*, \boldsymbol{t}^*\}$, is chosen by solving the following trivial optimization problem

$$\underset{z \in \{1,2,\ldots,6\}}{\text{minimize}} \quad J_z \,. \tag{16}$$

According to the receding horizon policy [3], only the switch positions that correspond to the first T_s are applied to the converter at the corresponding time instants, i.e.,

$$\begin{aligned} \boldsymbol{U}^*(k) &= \Big[\boldsymbol{u}^{*T}_{abc}(t_0(k))\ \boldsymbol{u}^{*T}_{abc}(t^*_1(k))\ \boldsymbol{u}^{*T}_{abc}(t^*_2(k))\ \boldsymbol{u}^{*T}_{abc}(t^*_3(k))\Big]^T \\ \boldsymbol{t}^*(k) &= \Big[t^*_1(k) \quad t^*_2(k) \quad t^*_3(k)\Big]^T . \end{aligned}$$

The block diagram of the proposed direct MPC scheme is shown in Fig. 4, and the pseudocode is provided in Algorithm 1.

D. Observer

MPC, being in essence a proportional controller, can be susceptible to steady-state tracking errors due to model uncertainties and variations, measurement noise, system non-idealities, such as dead-time effects, etc. [2]. To tackle this,

Algorithm 1 Fixed Switching Frequency Direct MPC

Given $\boldsymbol{u}_{abc}(t_0^-)$, $\boldsymbol{i}_{s,\mathrm{ref}}(t_0)$ and $\boldsymbol{x}(t_0)$
1: Compute the corresponding gradient vectors $\boldsymbol{m}_w$, $w \in \{0, 1, \ldots, 6\}$
2: Enumerate the possible switching sequences $\boldsymbol{U}_z$, $z \in \{1, 2, \ldots, 6\}$, based on $\boldsymbol{u}_{abc}(t_0^-)$
3: For each $\boldsymbol{U}_z$:
  Detect if $\boldsymbol{U}_z$ is unsuited;
  If not, solve the QP (15). This yields $\boldsymbol{t}_z$ and J_z.
4: Solve optimization problem (16). This yields $\boldsymbol{t}^*$ and $\boldsymbol{U}^*$.
Return $\boldsymbol{t}^*(k)$ and $\boldsymbol{U}^*(k)$.

an observer, such as a Kalman filter (KF), can enhance the robustness of MPC schemes to parameter mismatches and other disturbances, see, e.g., [31], [32]. To achieve a high degree of robustness as well as to obtain the rotor flux, a KF is implemented in this work. Based on the discrete-time state-space model (5), the KF equations are [33]

$$\begin{aligned} \hat{\boldsymbol{x}}(k+1|k) &= \boldsymbol{A}\hat{\boldsymbol{x}}(k) + \boldsymbol{B}\boldsymbol{u}_{abc}(k) \\ \boldsymbol{P}(k+1|k) &= \boldsymbol{A}\boldsymbol{P}(k|k)\boldsymbol{A}^T + \boldsymbol{Q} \\ \boldsymbol{L}(k+1) &= \boldsymbol{P}(k+1|k)\boldsymbol{C}^T(\boldsymbol{C}\boldsymbol{P}(k+1|k)\boldsymbol{C}^T + \boldsymbol{R})^{-1} \\ \hat{\boldsymbol{x}}(k+1|k+1) &= \hat{\boldsymbol{x}}(k+1|k) \\ &\quad + \boldsymbol{L}(k+1)(\boldsymbol{y}(k+1) - \boldsymbol{C}\hat{\boldsymbol{x}}(k+1|k)) \\ \boldsymbol{P}(k+1|k+1) &= \boldsymbol{P}(k+1|k) - \boldsymbol{L}(k+1)\boldsymbol{C}\boldsymbol{P}(k+1|k)\,, \end{aligned} \tag{17}$$

where $\boldsymbol{L}$ is the Kalman gain matrix, $\hat{\boldsymbol{x}}$ is the estimated state, $\boldsymbol{P}$ is the error covariance matrix, while $\boldsymbol{Q}$ and $\boldsymbol{R}$ are the system noise and measurement covariance matrices, respectively.

IV. Gradient Methods for Direct MPC

Gradient projection methods have shown to be very efficient for QPs, especially when the constraints are simple. In particular, they have been widely used for QPs where the variables of interest are only box-constrained [34]. For general QPs, projecting the variables onto the feasible region may require significant computations. However, the constraints

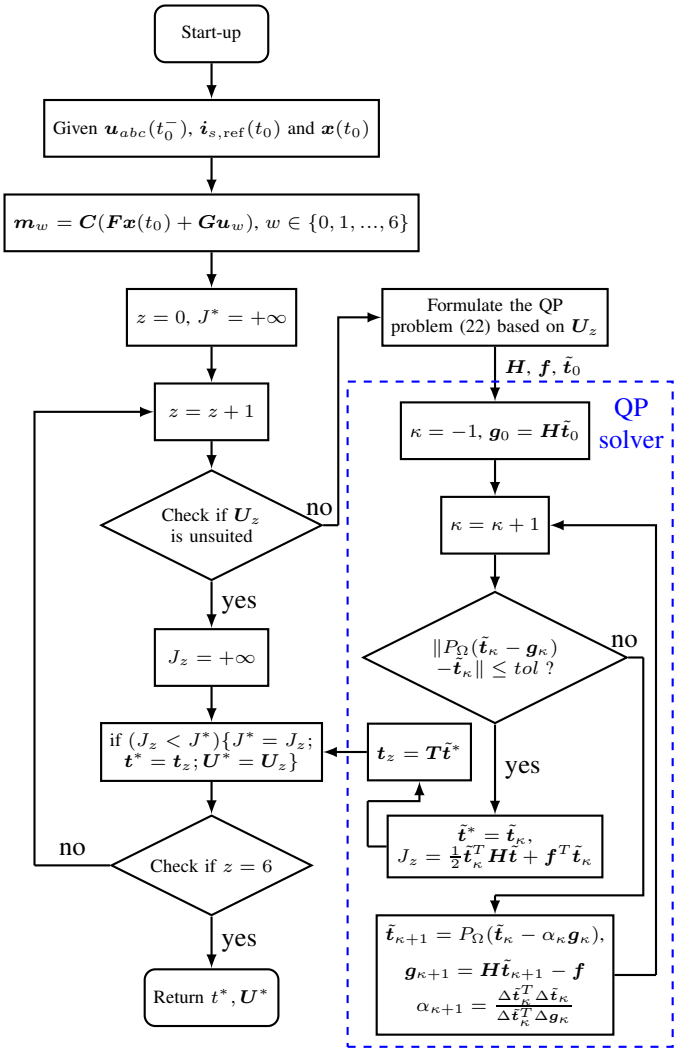

Fig. 5: Flowchart of the proposed fixed switching frequency direct MPC scheme.

in many MPC problems for power electronic systems are simple and regular (i.e., global), thus the projection onto the problem-specific feasible region can be efficiently performed by fully exploiting its geometry. In this section, we propose a computationally efficient projection method for the QP problem of the direct MPC discussed in Section III. The flowchart that summarizes the proposed gradient-based direct MPC scheme and the QP solver is shown in Fig. 5.

A. Reformulation of the Feasible Set

The feasible set of the QP problem (15) is a so-called truncated monotone cone. The projection of a variable onto a truncated monotone cone is complicated, see [35] and references therein. Although some algorithms exist, they rely on complex approaches, such as multiparametric programming [35], or involve computationally intensive operations, such as the computation of pseudo-inverses of matrices [36].

To address this and to achieve a computationally efficient projection, the feasible set is first reformulated by introducing the new variables $\tilde{t}_i = t_i - t_{i-1}$, with $i \in \{1, 2, 3, 4\}$ and $t_4 = T_s$. Note that $\tilde{t}_i$ is essentially the application time of the switch position $\boldsymbol{u}_{abc}(t_{i-1})$. In doing so, the feasible set can be described by simple bound constraints and one equality constraint, i.e., $\tilde{t}_i \geq 0$, and $\sum_{i=1}^4 \tilde{t}_i = T_s$. This concept can be applied to all variables involved in the long-horizon direct MPC problem.

Based on the above, the vector of application times is defined as

$$\tilde{\boldsymbol{t}} = \begin{bmatrix} \tilde{\boldsymbol{t}}^T(k) & \tilde{\boldsymbol{t}}^T(k+1) \end{bmatrix}^T \tag{18}$$

where

$$\tilde{\boldsymbol{t}}(\ell) = \begin{bmatrix} \tilde{t}_1(\ell) & \tilde{t}_2(\ell) & \tilde{t}_3(\ell) & \tilde{t}_4(\ell) \end{bmatrix}^T. \tag{19}$$

With (18), function (13) is rewritten as

$$J = \|\tilde{\boldsymbol{r}} - \tilde{\boldsymbol{M}}\tilde{\boldsymbol{t}}\|_2^2, \tag{20}$$

where the vector $\tilde{\boldsymbol{r}}$ and matrix $\tilde{\boldsymbol{M}}$ are provided in the appendix. After expanding (20) as

$$J = \tilde{\boldsymbol{t}}^T\tilde{\boldsymbol{M}}^T\tilde{\boldsymbol{M}}\tilde{\boldsymbol{t}} - 2\tilde{\boldsymbol{r}}^T\tilde{\boldsymbol{M}}\tilde{\boldsymbol{t}} + \tilde{\boldsymbol{r}}^T\tilde{\boldsymbol{r}} \tag{21}$$

and by omitting the constant term $\tilde{\boldsymbol{r}}^T\tilde{\boldsymbol{r}}$, the reformulated optimization problem can be stated as

$$\begin{aligned} \underset{\tilde{\boldsymbol{t}} \in \mathbb{R}^8}{\text{minimize}} \quad & \frac{1}{2}\tilde{\boldsymbol{t}}^T\boldsymbol{H}\tilde{\boldsymbol{t}} - \boldsymbol{f}^T\tilde{\boldsymbol{t}} \\ \text{subject to} \quad & \tilde{\boldsymbol{t}} \succeq \boldsymbol{0} \\ & \sum_{i=1}^4 \tilde{t}_i(\ell) = T_s, \ \forall \ell = k, k+1, \end{aligned} \tag{22}$$

where $\boldsymbol{H} = 2\tilde{\boldsymbol{M}}^T\tilde{\boldsymbol{M}}$ is a symmetric, positive (semi)definite matrix, $\boldsymbol{f} = 2\tilde{\boldsymbol{M}}^T\tilde{\boldsymbol{r}}$, $\boldsymbol{0}$ is a zero vector of appropriate dimensions, and $\succeq$ denotes componentwise inequality. Note that after the QP problem (22) has been solved, the switching time instants $\boldsymbol{t}$ can be simply calculated as

$$\boldsymbol{t} = \boldsymbol{T}\tilde{\boldsymbol{t}}, \tag{23}$$

where the transformation matrix $\boldsymbol{T}$ is provided in the appendix.

B. Projection onto the Feasible Region

An important step in gradient methods for constrained QP problems is the projection of the variables of interest onto the feasible region. Let the feasible region of (22) be defined as

$$\Omega := \{\tilde{\boldsymbol{t}} \mid \tilde{\boldsymbol{t}} \succeq \boldsymbol{0}, \sum_{i=1}^4 \tilde{t}_i = \sum_{i=5}^8 \tilde{t}_i = T_s, \tilde{\boldsymbol{t}} \in \mathbb{R}^8\}.$$

The projection of any vector $\boldsymbol{z}$ onto Ω is the minimizer of the problem

$$\underset{\tilde{\boldsymbol{\tau}} \in \Omega}{\text{minimize}} \quad \|\tilde{\boldsymbol{\tau}} - \boldsymbol{z}\|_2^2. \tag{24}$$

The proposed projection algorithm is based on constructing the associated Lagrangian of (24), i.e.,

$$\begin{aligned} &\mathcal{L}(\tilde{\boldsymbol{\tau}}, \lambda_1, \lambda_2, \boldsymbol{\mu}) = \\ &\frac{1}{2}\tilde{\boldsymbol{\tau}}^T\tilde{\boldsymbol{\tau}} - \boldsymbol{z}^T\tilde{\boldsymbol{\tau}} - \lambda_1(\boldsymbol{a}_1^T\tilde{\boldsymbol{\tau}} - T_s) - \lambda_2(\boldsymbol{a}_2^T\tilde{\boldsymbol{\tau}} - T_s) - \boldsymbol{\mu}^T\tilde{\boldsymbol{\tau}}, \end{aligned} \tag{25}$$

where $\lambda_1, \lambda_2 \in \mathbb{R}$ and $\boldsymbol{\mu} \in \mathbb{R}^8$ are the so-called Lagrangian multipliers. Moreover, $\boldsymbol{a}_1 = [\boldsymbol{1}_4^T \ \boldsymbol{0}_4^T]^T$ and $\boldsymbol{a}_2 = [\boldsymbol{0}_4^T \ \boldsymbol{1}_4^T]^T$

are the vectors of the equality constraints, where $\mathbf{0}$ and $\mathbf{1}$ are vectors with all components being zero and one, respectively, and of dimension indicated by their subscript. The first-order necessary conditions, which are known as the Karush-Kuhn-Tucker (KKT) conditions, state that if $\tilde{\boldsymbol{\tau}}^*$, i.e., the projection point, is a local solution of (24), then there is a set of Lagrangian multipliers $\{\boldsymbol{\mu}^*, \lambda_1^*, \lambda_2^*\}$, such that the following conditions are satisfied at $(\tilde{\boldsymbol{\tau}}^*, \lambda_1^*, \lambda_2^*, \boldsymbol{\mu}^*)$ [34]

$$\tilde{\boldsymbol{\tau}}^* - \boldsymbol{z} - \lambda_1^* \boldsymbol{a}_1 - \lambda_2^* \boldsymbol{a}_2 - \boldsymbol{\mu}^* = \mathbf{0}\,, \tag{26a}$$

$$\tilde{\boldsymbol{\tau}}^* \succeq \mathbf{0},\ \boldsymbol{\mu}^* \succeq \mathbf{0}\,, \tag{26b}$$

$$\tilde{\boldsymbol{\tau}}^* \odot \boldsymbol{\mu}^* = \mathbf{0}\,, \tag{26c}$$

$$\boldsymbol{a}_1^T \tilde{\boldsymbol{\tau}}^* = T_s,\ \boldsymbol{a}_2^T \tilde{\boldsymbol{\tau}}^* = T_s\,, \tag{26d}$$

where $\odot$ denotes the componentwise product. For the convex QP (24) satisfaction of the KKT conditions (26) suffices for $\tilde{\boldsymbol{\tau}}^*$ to be a global solution [37]. In the following, it is shown how $\tilde{\boldsymbol{\tau}}^*$ can be found by solving the KKT conditions (26).

First, it is noted that (26) can be split into two decoupled sets of equations[3]

$$\tilde{\boldsymbol{\tau}}^*_{(4\zeta-3:4\zeta)} - \boldsymbol{z}_{(4\zeta-3:4\zeta)} - \lambda_\zeta^* \mathbf{1}_4 - \boldsymbol{\mu}^*_{(4\zeta-3:4\zeta)} = \mathbf{0}\,, \tag{27a}$$

$$\tilde{\boldsymbol{\tau}}^*_{(4\zeta-3:4\zeta)} \succeq \mathbf{0},\ \boldsymbol{\mu}^*_{(4\zeta-3:4\zeta)} \succeq \mathbf{0}\,, \tag{27b}$$

$$\tilde{\boldsymbol{\tau}}^*_{(4\zeta-3:4\zeta)} \odot \boldsymbol{\mu}^*_{(4\zeta-3:4\zeta)} = \mathbf{0}\,, \tag{27c}$$

$$\sum_{i=4\zeta-3}^{4\zeta} \tilde{\tau}_i^* = T_s\,, \tag{27d}$$

where the value of $\zeta \in \{1, 2\}$ indicates the prediction horizon step. Therefore, the two equation sets (27) can be solved separately. By taking $\zeta = 1$ as an example, (27a) can be expanded to four scalar equations as

$$\tilde{\tau}_i = z_i + \lambda_1 + \mu_i,\ i \in \{1, 2, 3, 4\}\,. \tag{28}$$

Combining (28) with (27b) and (27c), it yields

$$(\tilde{\tau}_i,\ \mu_i) = \begin{cases} (0,\ -\lambda_1 - z_i) & \text{if} \quad \lambda_1 < -z_i \\ (z_i + \lambda_1,\ 0) & \text{otherwise}\,. \end{cases} \tag{29}$$

If there exists λ_1 such that $\sum_{i=1}^4 \tilde{\tau}_i^* = T_s$—denoted as λ_1^*—it follows that the KKT conditions (26) with $\zeta = 1$ are satisfied. As a result, the solution $\tilde{\boldsymbol{\tau}}^*_{(1:4)}$ can be obtained directly from (29). Specifically, based on (29), $\sum_{i=1}^4 \tilde{\tau}_i$ can be written as a piecewise linear continuous function of λ_1

$$f(\lambda_1) = \sum_{i=1}^4 \tilde{\tau}_i = \begin{cases} 0 & \text{if } \lambda_1 < -\tilde{z}_1 \\ \tilde{z}_1 + \lambda_1 & \text{if } -\tilde{z}_1 \le \lambda_1 < -\tilde{z}_2 \\ \vdots & \\ \sum_{i=1}^4 \tilde{z}_i + 4\lambda_1 & \text{if } -\tilde{z}_4 \le \lambda_1\,, \end{cases} \tag{30}$$

where $\tilde{\boldsymbol{z}}$ includes the elements of $\boldsymbol{z}$ sorted in a descending order. Since $f(\lambda_1)$ is either constant or increasing monotonically and linearly with λ_1, λ_1^* can be found by examining the value of $f(\lambda_1)$ at its breakpoints $\tilde{\lambda}_i$. From (30), it is evident that $f(\lambda_1)$ has four breakpoints, i.e., $\tilde{\lambda}_i = -\tilde{z}_i$ for $i \in \{1, 2, 3, 4\}$. Once a $\tilde{\lambda}_j$ is found such that $f(\tilde{\lambda}_{j-1}) \le T_s$ and $f(\tilde{\lambda}_j) \ge T_s$, then λ_1^* is in the interval $[\tilde{\lambda}_{j-1}, \tilde{\lambda}_j]$ and can be obtained by linear interpolation. If λ_1^* is not found after all the breakpoints are examined, then λ_1^* is located in the interval $[\tilde{\lambda}_4, +\infty)$ and it is equal to $\lambda_1^* = (T_s - \sum_{i=1}^4 \tilde{z}_i)/4$.

Once λ_1^* and $\tilde{\boldsymbol{\tau}}^*_{(1:4)}$ are obtained, λ_2^* and $\tilde{\boldsymbol{\tau}}^*_{(5:8)}$ can be found by setting $\zeta = 2$ and following the same procedure. The proposed projection algorithm is summarized in Algorithm 2.

[3]The notation $\tilde{\boldsymbol{\tau}}^*_{(4\zeta-3:4\zeta)}$, $\boldsymbol{z}_{(4\zeta-3:4\zeta)}$, and $\boldsymbol{\mu}^*_{(4\zeta-3:4\zeta)}$ indicates the entries from $4\zeta - 3$ up to 4ζ of $\tilde{\boldsymbol{\tau}}^*$, $\boldsymbol{z}$, and $\boldsymbol{\mu}^*$, respectively.

Algorithm 2 Projection onto Ω

function $\tilde{\boldsymbol{\tau}}^* = P_\Omega(\boldsymbol{z})$
  for $\zeta = 1,\ 2$ **do**
    $\tilde{\boldsymbol{z}} = \mathrm{sort}(\boldsymbol{z}_{(4\zeta-3:4\zeta)}, \mathrm{descend})$
    $\tilde{\boldsymbol{\lambda}} = -\tilde{\boldsymbol{z}}$
    $f(\tilde{\lambda}_1) = 0$
    for $j = 2$ to 4 **do**
      $f(\tilde{\lambda}_j) = \sum_{i=1}^j \tilde{z}_i + j\tilde{\lambda}_j$
      if $f(\tilde{\lambda}_j) \ge T_s$ **then**
        $\lambda_\zeta^* = \tilde{\lambda}_{j-1} + (\tilde{\lambda}_j - \tilde{\lambda}_{j-1})\frac{(T_s - f(\tilde{\lambda}_{j-1}))}{(f(\tilde{\lambda}_j) - f(\tilde{\lambda}_{j-1}))}$
        break
      else
        if $j = 4$ **then**
          $\lambda_\zeta^* = (T_s - \sum_{i=1}^4 \tilde{z}_i)/4$
          break
        end if
      end if
    end for
    $\tilde{\boldsymbol{\tau}}^*_{(4\zeta-3:4\zeta)} = \max\{\mathbf{0}_4, \boldsymbol{z}_{(4\zeta-3:4\zeta)} + \lambda_\zeta^* \mathbf{1}_4\}$
  end for
  return $\tilde{\boldsymbol{\tau}}^*$
end function

C. Gradient Projection Method for Direct MPC

To find the solution $\tilde{\boldsymbol{t}}^*$ of problem (22), the proposed gradient projection method searches along the steepest descent direction from the current point $\tilde{\boldsymbol{t}}_\kappa$, i.e.,

$$\tilde{\boldsymbol{t}}_{\kappa+1} = \tilde{\boldsymbol{t}}_\kappa - \alpha_\kappa \boldsymbol{g}_\kappa\,, \tag{31}$$

where $\boldsymbol{g}_\kappa = \boldsymbol{H}\tilde{\boldsymbol{t}}_\kappa - \boldsymbol{f}$ is the gradient vector at $\tilde{\boldsymbol{t}}_\kappa$, $\alpha_\kappa \in \mathbb{R}^+$ is the step size, and $\kappa \in \mathbb{N}$ denotes the κ^{th} step of the solution process. Following, $\tilde{\boldsymbol{t}}_{\kappa+1}$ is projected onto the feasible region Ω by invoking Algorithm 2, i.e., $\tilde{\boldsymbol{\tau}}^*_{\kappa+1} = P_\Omega(\tilde{\boldsymbol{t}}_{\kappa+1})$, where P_Ω refers to the projection function provided in Algorithm 2. Subsequently, the process continues from point $\tilde{\boldsymbol{\tau}}^*_{\kappa+1}$ by considering it as the next starting point in (31), i.e., $\tilde{\boldsymbol{t}}_{\kappa+1} \equiv \tilde{\boldsymbol{\tau}}^*_{\kappa+1}$.

As can be understood, an important factor that affects the rate of convergence of the gradient method is the step size α_κ. In the classic steepest descent method this is chosen by exact line search, i.e., by searching for the optimal point along the steepest descent direction. However, it has been shown that the rate of convergence of the classical method is slow and it gets worse as the QP problem becomes ill-posed. As an alternative, Barzilai and Borwein proposed a strategy—known as the BB method—for choosing the step size [38], which

Algorithm 3 QP Algorithm for Direct MPC

function $\tilde{\boldsymbol{t}}^* = \textsc{GradProj}(\boldsymbol{H}, \boldsymbol{f}, \tilde{\boldsymbol{t}}_0, \alpha_0, tol)$
  $\boldsymbol{g}_0 = \boldsymbol{H}\tilde{\boldsymbol{t}}_0 - \boldsymbol{f}$
  for $\kappa = 0,\ 1,\ \ldots$ **do**
    if $\|P_\Omega(\tilde{\boldsymbol{t}}_\kappa - \boldsymbol{g}_\kappa) - \tilde{\boldsymbol{t}}_\kappa\| \leq tol$ **then**
      $\tilde{\boldsymbol{t}}^* = \tilde{\boldsymbol{t}}_\kappa$
      break
    end if
    $\tilde{\boldsymbol{\tau}}^*_{\kappa+1} = P_\Omega(\boldsymbol{t}_\kappa - \alpha_\kappa \boldsymbol{g}_\kappa)$
    $\tilde{\boldsymbol{t}}_{\kappa+1} = \tilde{\boldsymbol{\tau}}^*_{\kappa+1}$
    $\boldsymbol{g}_{\kappa+1} = \boldsymbol{H}\tilde{\boldsymbol{t}}_{\kappa+1} - \boldsymbol{f}$
    $\alpha_{\kappa+1} = (\Delta\tilde{\boldsymbol{t}}_\kappa^T \Delta\tilde{\boldsymbol{t}}_\kappa)/(\Delta\tilde{\boldsymbol{t}}_\kappa^T \Delta\boldsymbol{g}_\kappa)$
  end for
  return $\tilde{\boldsymbol{t}}^*$
end function

offers several advantages over the classical method, such as less computational effort, fast convergence, and less sensitivity to ill conditioning [39], [40]. According to the BB step [38], the step size in (31) is chosen as

$$\alpha_{\kappa+1} = \frac{\Delta\tilde{\boldsymbol{t}}_\kappa^T \Delta\tilde{\boldsymbol{t}}_\kappa}{\Delta\tilde{\boldsymbol{t}}_\kappa^T \Delta\boldsymbol{g}_\kappa}\,, \tag{32}$$

where $\Delta\tilde{\boldsymbol{t}}_\kappa = \tilde{\boldsymbol{t}}_{\kappa+1} - \tilde{\boldsymbol{t}}_\kappa$ and $\Delta\boldsymbol{g}_\kappa = \boldsymbol{g}_{\kappa+1} - \boldsymbol{g}_\kappa$. With (31) and (32), the algorithm continuous in an iterative manner until it fulfills an optimization criterion. Specifically, the process terminates when $\|P_\Omega(\tilde{\boldsymbol{t}}_\kappa - \boldsymbol{g}_\kappa) - \tilde{\boldsymbol{t}}_\kappa\|$ is within a predetermined tolerance.

Based on the above, the complete algorithm for solving (22) is summarized in Algorithm 3. The arguments of the algorithm are the Hessian matrix $\boldsymbol{H}$, and the vector $\boldsymbol{f}$, as defined in (22) as well as the initial point $\tilde{\boldsymbol{t}}_0 \in \Omega$, the initial step α_0, and the value of the tolerance tol. The initial point can be chosen according to a warm-start strategy, e.g., based on the previously computed solution $\tilde{\boldsymbol{t}}^*(k+1)$. Moreover, in this work, as shown in Section IV-D, $\tilde{\boldsymbol{t}}_0$ is also utilized for detecting unsuited switching sequences $\boldsymbol{U}$. As for the initial step size α_0, it marginally affects the convergence of the algorithm, since it is updated in every iteration of the search process according to (32). On the other hand, the tolerance tol can considerably affect the rate of convergence, since a very small value can result in a slow convergence. However, the exact solution is not necessary since the model itself is not ideal. Hence, in this work, tol is set to 10^{-6}, which means that the optimal switching application times $\tilde{\boldsymbol{t}}^*$ are acceptable within a tolerance of 1 µs. Considering that the sampling interval for the examined case study is a few hundreds of microseconds, a solution with 1 µs tolerance is accurate enough.

Finally, it is worth mentioning that the BB methods are inherently non-monotonic, which means that the value of the objective function may increase at some iterations. To tackle this, a line search is required to prove the convergence, and some studies, e.g., [41], have reported some cases that the BB methods without line search fail to converge. However, this happens rarely and only in large-scale problems. For small-scale QPs, as the one presented in (22), the employed BB method always converges efficiently without requiring a line search. For more details about the line search strategy, see [39] and references therein.

D. Detection of Unsuited Switching Sequences

As explained in Section III, the gradient-based direct MPC scheme enumerates the feasible switching sequences and selects the one that minimizes (16). According to the control principle presented in Section III-A, each switching sequence in one sampling interval T_s consists of four switch positions; two of them correspond to zero vectors in the $\alpha\beta$-plane—applied at the beginning and end of T_s—and the other two to adjacent active vectors—applied in between, see Fig. 2(a). However, not all active vectors positively affect the tracking of the stator current reference. Such active vectors, and consequently the corresponding switching sequences, can be detected quickly by the proposed gradient projection method, as explained below.[4]

To do so, consider one-step MPC and let the initial point be $\tilde{\boldsymbol{t}}_0 = [T_s/2\ 0\ 0\ T_s/2]$. The steepest descent direction can be obtained by calculating its gradient vector $\boldsymbol{g}_0 = \boldsymbol{H}\tilde{\boldsymbol{t}}_0 - \boldsymbol{f}$. If this direction points to the region where $\tilde{\boldsymbol{t}}$ has negative duration time for an active vector, i.e., the second and third entries of $\tilde{\boldsymbol{t}}$, it can be concluded that this active vector will adversely affect the system performance if applied to the inverter, thus the associated switching sequence is suboptimal.

To allow the gradient projection to reach the region where $\tilde{t}_i < 0$, the bound constraints are neglected so that the *relaxed* feasible region is defined as

$$\Omega_0 \coloneqq \{\tilde{\boldsymbol{t}} \mid \sum_{i=1}^{4} \tilde{t}_i = T_s, \tilde{\boldsymbol{t}} \in \mathbb{R}^4\}\,.$$

Then, one step is taken from the initial point $\tilde{\boldsymbol{t}}_0$ in the steepest descent direction and projected onto the relaxed region, i.e., $\tilde{\boldsymbol{t}}_1 = P_{\Omega_0}(\tilde{\boldsymbol{t}}_0 - \boldsymbol{g}_0)$, where $P_{\Omega_0}(\boldsymbol{z})$ is the function that projects any vector $\boldsymbol{z}$ onto Ω_0. If the duration of an active vector in $\tilde{\boldsymbol{t}}_1$ is negative, the associated switching sequence is discarded. The projection $P_{\Omega_0}(\boldsymbol{z})$, is computed as

$$\underset{\tilde{\boldsymbol{\tau}} \in \Omega_0}{\text{minimize}} \quad \|\tilde{\boldsymbol{\tau}} - \boldsymbol{z}\|_2^2\,, \tag{33}$$

which can be easily solved by exploring its KKT conditions, i.e.,

$$\tilde{\boldsymbol{\tau}}^* - \boldsymbol{z} - \lambda^* \mathbf{1}_4 = \mathbf{0}\,, \tag{34a}$$

$$\sum_{i=1}^{4} \tilde{\tau}_i^* = T_s\,. \tag{34b}$$

Specifically, since (34a) can be written as $\tilde{\tau}_i^* = z_i + \lambda^*$, $i \in \{1,2,3,4\}$, by inserting it into (34b), the solution of (33) is given by $\lambda^* = (T_s - \sum_{i=1}^4 z_i)/4$ and $\tilde{\boldsymbol{\tau}}^* = \lambda^* \mathbf{1}_4 + \boldsymbol{z}$. Hence, $\tilde{\boldsymbol{t}}_1$ can be found with a simple one-step projection, enabling a fast and accurate detection of unsuited switching sequences.

[4] An alternative to determine the "suitable" switching sequence is to utilize the deadbeat solution of the control problem, i.e., the modulating signal that a deadbeat controller would use. In doing so, the triangular sector in which the modulating signal lies would provide the desired switching sequence, see Fig. 3. However, such an approach can lead to suboptimal solutions [4, Section VII], thus the proposed method is preferred since it guarantees optimality.

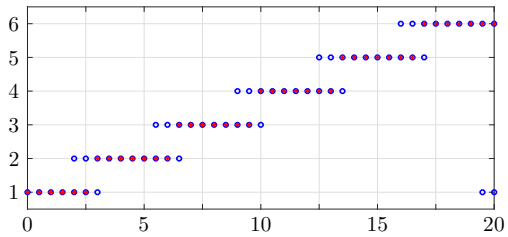

(a) Steady-state operation.

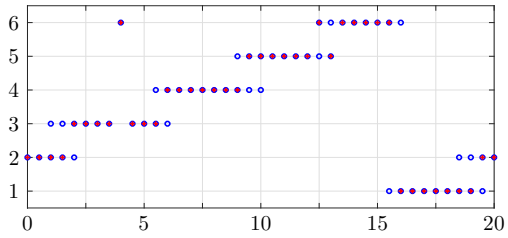

(b) Transient operation.

Fig. 6: Switching sequences selected by the detection method (blue circles) and the globally optimal switching sequence (red cross).

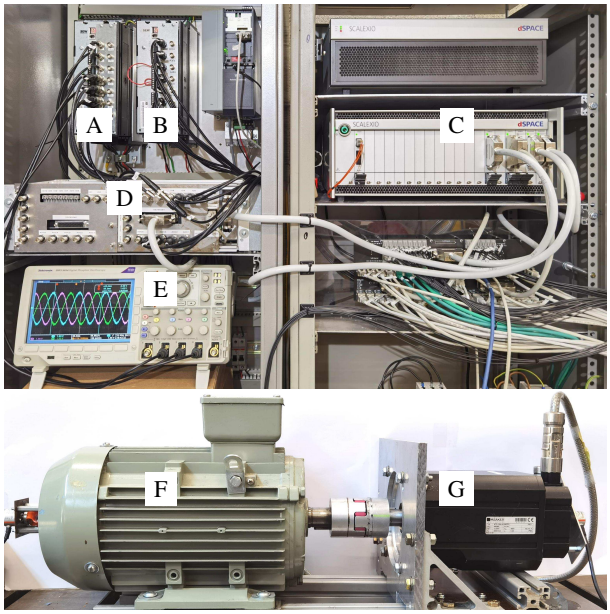

Fig. 7: Experimental setup of the electrical drive test bench. A: SEW inverter for induction machine (IM), B: SEW inverter for load permanent magnet synchronous machine (PMSM), C: dSPACE SCALEXIO real-time control system, D: Interface, E: Oscilloscope, F: IM, G: PMSM.

The validity of the described method is examined in simulation for both steady-state and transient operation for the drive system shown in Fig. 1 with the parameters given in Tables II and III. Fig. 6(a) shows for one fundamental period the switching sequences $\boldsymbol{U}_z$, $z \in \{1, 2, \ldots, 6\}$, (see Table I) considered as candidate solutions (shown as blue circles) by the aforementioned method in steady-state operation. In the same figure, the optimal switching sequence $\boldsymbol{U}^*$ found after solving all six QPs for all possible switching sequences is also indicated (shown with a red cross). Moreover, the same data are depicted in Fig. 6(b) for transient operation, namely for a torque reference step-down—from $T_{e,\mathrm{ref}} = 1$ to 0 per unit (p.u.)—and step-up—from $T_{e,\mathrm{ref}} = 0$ to 1 p.u.—change at $t = 4$ ms and $t = 13$ ms, respectively. As can be seen, the detection method selects one or two "suitable" switching sequences, with the globally optimal sequence always included.

V. Performance Evaluation

The performance of the proposed direct MPC scheme is examined in the laboratory with a three-phase two-level inverter driving an IM, as shown in Fig. 1. The inverter is supplied by a stiff dc source. The real-time control platform is a dSPACE SCALEXIO system, consisting of a 4 GHz Intel XEON processor and a Xilinx Kintex-7 field-programmable gate array (FPGA). Two three-phase two-level SEW MDX inverters are used to control the IM and the load machine. The experimental setup is shown in Fig. 7. The rated values of the IM and the parameters of the system are given in Tables II and III, respectively. Note that all results are shown in the p.u. system.

A. Steady-State Operation

The steady-state performance of the drive system controlled by the direct MPC scheme is examined while the IM is operating at rated torque and nominal speed, i.e., the fundamental frequency is $f_1 = 50$ Hz, and the electromagnetic torque reference is set equal to $T_{e,\mathrm{ref}} = 1$ p.u., as shown in Fig. 8. Considering that the relationship between the switching frequency f_{sw} and the sampling interval T_s is given by

$$f_{\mathrm{sw}} = \frac{1}{2T_s}, \tag{35}$$

the sampling interval is chosen as $T_s = 123.4\,\mu$s so that a switching frequency f_{sw} of 4050 Hz results. Fig. 8(a) shows the three phase stator current measured by the oscilloscope with a sampling frequency of 50 kHz, while its harmonic spectrum is shown in Fig. 8(b). The current THD is 5.80%, relatively low considering the small total leakage reactance of 0.11 p.u. The current harmonics are mainly the sideband harmonics caused by the switching nature of the converter. Besides, some pronounced harmonics can be observed at low frequencies, especially around 1000 Hz, i.e., the 17$^{\mathrm{th}}$ and

TABLE II: Rated values of the induction machine.

Parameter	Symbol	SI Value
Rated voltage	V_R	380 V
Rated current	I_R	5.73 A
Rated stator frequency	f_{sR}	50 Hz
Rated rotor speed	ω_{mR}	2880 rpm
Rated power	P_R	3 kW

TABLE III: System parameters in the SI and the p.u. system.

Parameter	SI (p.u.) symbol	SI (p.u.) value
Stator resistance	R_s (R_s)	1.509 Ω (0.0394)
Rotor resistance	R_r (R_r)	1.235 Ω (0.0323)
Stator leakage inductance	L_{ls} (X_{ls})	7.0 mH (0.0574)
Rotor leakage inductance	L_{lr} (X_{lr})	7.0 mH (0.0574)
Mutual inductance	L_m (X_m)	232.5 mH (1.9077)
Number of pole pairs	p	1
Dc-link voltage	V_{dc} (V_{dc})	650 V (2.0950)

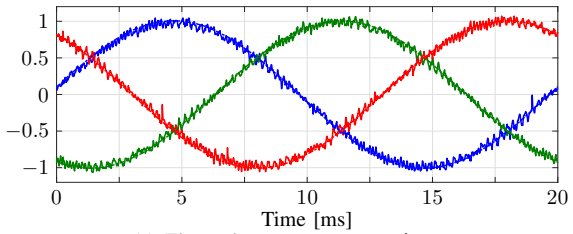

(a) Three-phase stator current $\boldsymbol{i}_{s,abc}$.

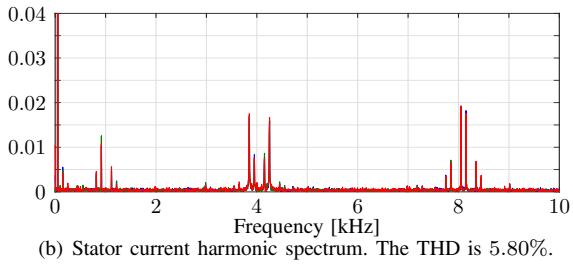

(b) Stator current harmonic spectrum. The THD is 5.80%.

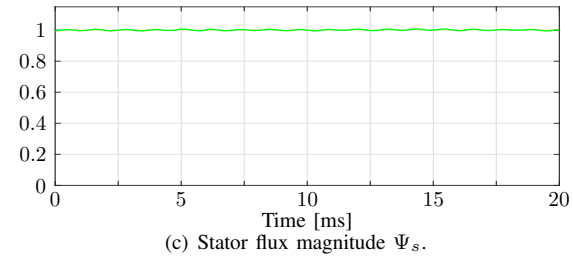

(c) Stator flux magnitude Ψ_s.

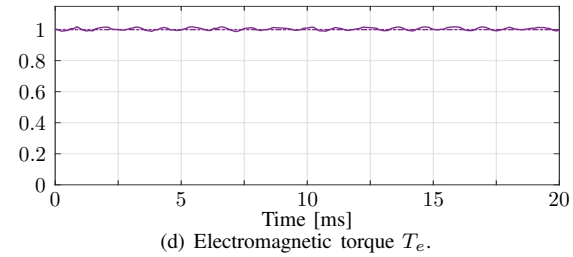

(d) Electromagnetic torque T_e.

Fig. 8: Experimental results of direct MPC at steady-state operation, $f_{\text{sw}} = 4050\,\text{Hz}$.

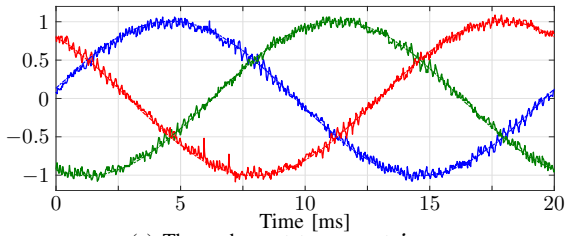

(a) Three-phase stator current $\boldsymbol{i}_{s,abc}$.

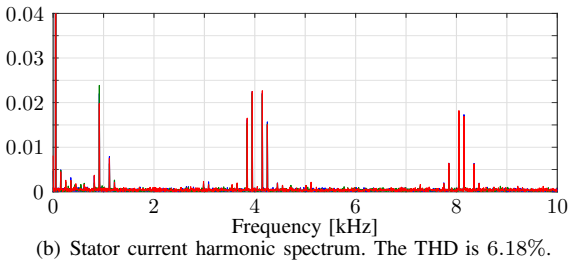

(b) Stator current harmonic spectrum. The THD is 6.18%.

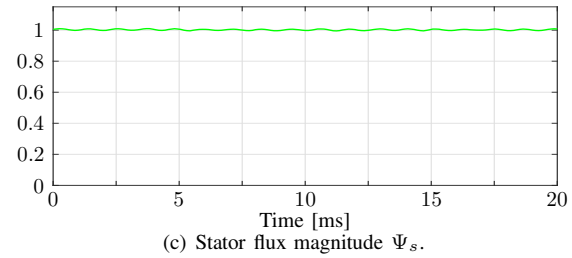

(c) Stator flux magnitude Ψ_s.

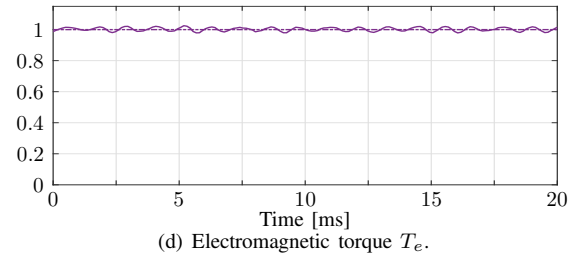

(d) Electromagnetic torque T_e.

Fig. 9: Experimental results of FOC at steady-state operation, $f_{\text{sw}} = 4050\,\text{Hz}$.

19^{th} harmonic. Such harmonics are mainly caused by the slotting and saturation effects in the IM [42]. Finally, Figs. 8(c) and 8(d) show the stator flux magnitude and electromagnetic torque, respectively. These values are estimated in dSPACE, based on the machine model and the observer discussed in Section III-D.

For comparison purposes, field-oriented control (FOC) with proportional-integral (PI) controllers and SVM is also implemented. The operating conditions and switching frequency are the same as those of direct MPC, while the PI parameters are tuned according to the modulus optimum method. As can be seen in Fig. 9(a), the stator current is very similar to that of the direct MPC scheme, but with a slightly higher ripple. This is reflected in the harmonic spectrum (see Fig. 9(b)), where higher current distortions can be observed, with the current THD being equal to 6.19%. This is mainly due to fact that the harmonics caused by the slotting and saturation effects are more pronounced with FOC. This can be explained by the fact that the PI-based FOC has less control bandwidth so it cannot effectively remove these relatively high-order harmonics. Conversely, MPC can suppress—to some extent—those harmonics caused by the nonlinearities of the IM.

Furthermore, to gain more insight into how the direct MPC scheme manipulates the converter switch positions, the notion of the three-phase equivalent modulating signal $\boldsymbol{d}_{abc}$ is introduced. To this end, the single-phase equivalent modulating signal is defined as $d_x = T_{\text{on},x}/T_s$, with $x \in \{a, b, c\}$, where $T_{\text{on},x}$ is the time interval within one T_s that $u_x = 1$. The three-phase equivalent modulating signal is shown in Fig. 10 for the proposed MPC scheme. In the same figure the modulating signal of FOC with SVM is depicted. As can be observed in Fig. 10, the direct MPC scheme, although it does not employ a modulator, achieves a very similar equivalent modulating signal.

Finally, to further elucidate the performance of the proposed controller, Fig. 11 depicts the current THD for switching frequencies in the range $f_{\text{sw}} \in [750, 5250]\,\text{Hz}$. As before, the current THD produced by FOC is also shown. Moreover,

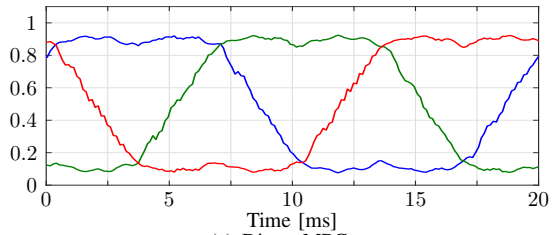

(a) Direct MPC.

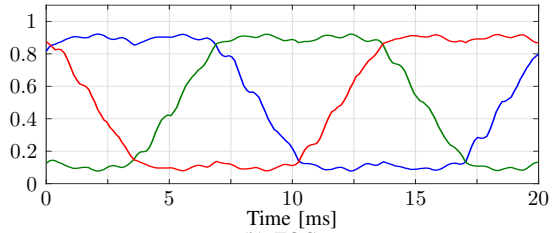

(b) FOC.

Fig. 10: Three phase equivalent modulating signal of direct MPC and modulating signal of FOC at nominal steady-state operation, $f_{\mathrm{sw}} = 4050\,\mathrm{Hz}$.

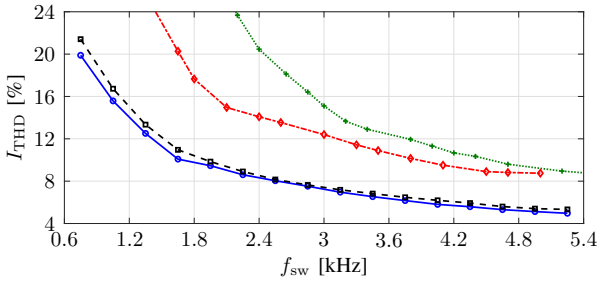

Fig. 11: Trade-off between current THD and switching frequency for the proposed direct MPC (blue, solid line), FOC (black, dashed line), FCS-MPC1 (green, dotted line), and FCS-MPC2 (red, dash-dotted line).

to clearly highlight the benefits of the proposed direct MPC strategy, the current THD achieved with two conventional FCS-MPC methods is also reported. Specifically, the first FCS-MPC method (referred to as FCS-MPC1) has the objective function

$$J = \|\boldsymbol{i}_{s,\mathrm{ref}}(k+1) - \boldsymbol{i}_s(k+1)\|_1\,,$$

i.e., it does not penalize the control action and uses the ℓ_1-norm, while the switching frequency is adjusted by modifying the sampling interval T_s. The objective function of the second FCS-MPC method (FCS-MPC2) is based on the ℓ_2-norm, penalizes the control effort, and uses the sampling interval $T_s = 50\,\mu\mathrm{s}$, i.e.,[5]

$$J = \|\boldsymbol{i}_{s,\mathrm{ref}}(k+1) - \boldsymbol{i}_s(k+1)\|_2^2 + \lambda_u \|\Delta \boldsymbol{u}_{abc}(k)\|_2^2\,.$$

As can be seen, Fig. 11 clearly shows the superior steady-state performance of the proposed direct MPC scheme since it achieves the lowest values of current THD I_{THD} over the whole range of the examined switching frequencies.

B. Transient Behavior

While operating at the same switching frequency as before (i.e., $f_{\mathrm{sw}} = 4050\,\mathrm{Hz}$), the transient behavior of the examined

[5]The reader is referred to [4] for insights into the discussed designs of FCS-MPC.

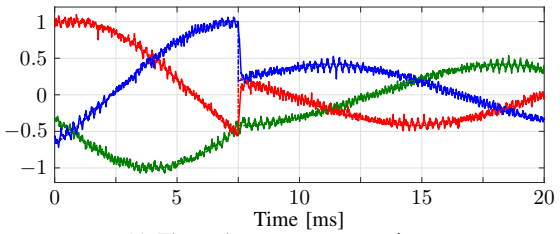

(a) Three-phase stator current $\boldsymbol{i}_{s,abc}$.

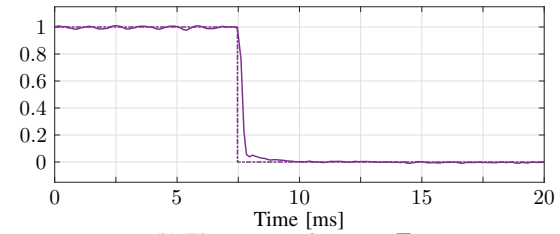

(b) Electromagnetic torque T_e.

Fig. 12: Experimental results of direct MPC during a torque reference step-down transient.

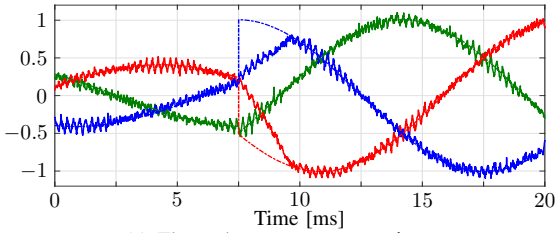

(a) Three-phase stator current $\boldsymbol{i}_{s,abc}$.

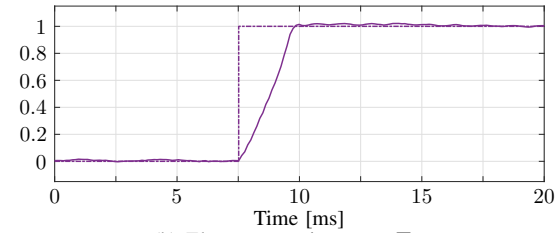

(b) Electromagnetic torque T_e.

Fig. 13: Experimental results of direct MPC during a torque reference step-up transient.

direct MPC scheme is tested during torque reference steps from $T_{e,\mathrm{ref}} = 1$ to 0 p.u. as well as from $T_{e,\mathrm{ref}} = 0$ to 1 p.u.. These cases are shown in Figs. 12 and 13, respectively. As a comparison, Figs. 14 and 15 show the performance of FOC for the same scenarios. For the torque reference step-down case, the proposed direct MPC scheme smoothly regulates the current—and thus the torque—to the new reference within two sampling intervals, without any over- and/or undershoots, see Fig. 12. FOC, on the other hand, suffers from a visible undershoot in the torque, see Fig. 14. As for the torque reference step-up case, the proposed direct MPC strategy achieves a significantly faster settling time of about 2 ms as compared to the 3 ms required by FOC, see Figs. 13 and 15, respectively.

For more insight into the dynamic behavior of the presented direct MPC algorithm, Fig. 16 shows the equivalent modulating signal during the torque reference step changes in detail.

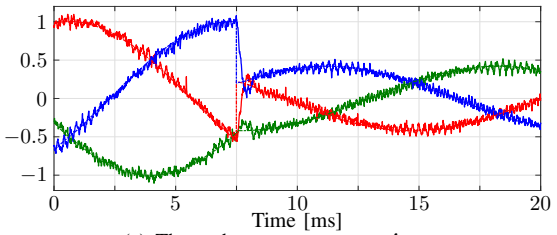

(a) Three-phase stator current $\boldsymbol{i}_{s,abc}$.

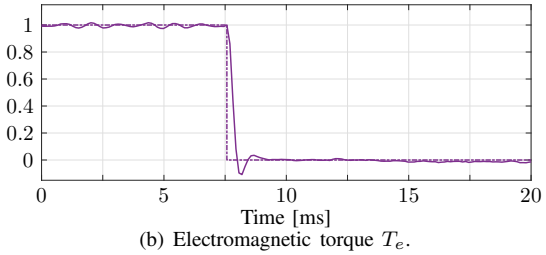

(b) Electromagnetic torque T_e.

Fig. 14: Experimental results of FOC during a torque reference step-down transient.

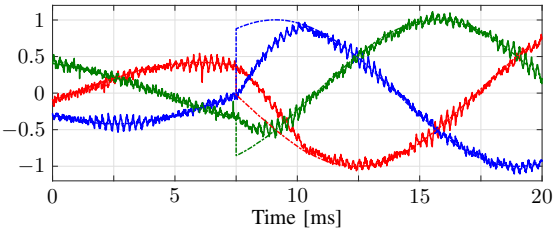

(a) Three-phase stator current $\boldsymbol{i}_{s,abc}$.

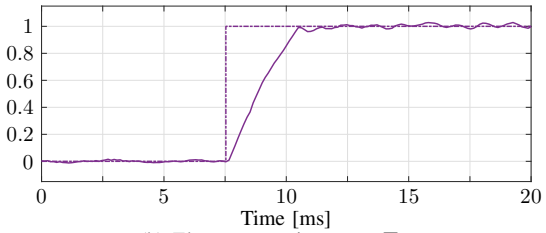

(b) Electromagnetic torque T_e.

Fig. 15: Experimental results of FOC during a torque reference step-up transient.

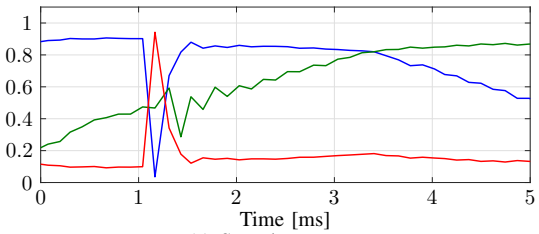

(a) Step-down case.

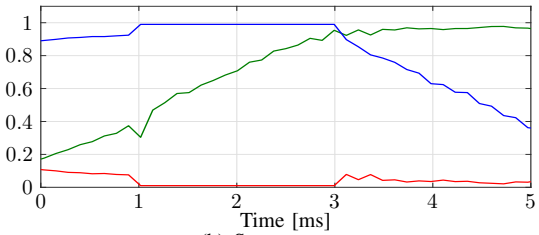

(b) Step-up case.

Fig. 16: Three-phase equivalent modulating signal of direct MPC at torque reference steps.

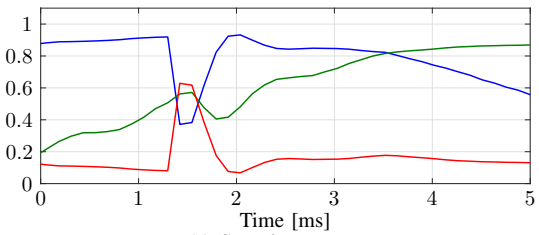

(a) Step-down case.

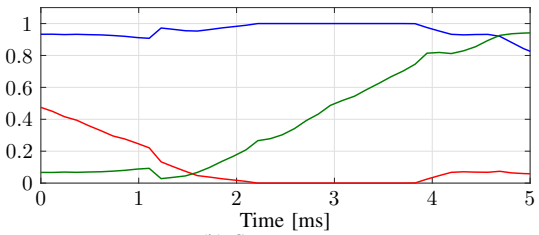

(b) Step-up case.

Fig. 17: Three-phase modulating signals of FOC at torque step reference steps.

In a same fashion, Fig. 17 depicts the modulating signal with FOC. At the torque reference step-down case, the direct MPC method instantly pushes the application times of the switch positions close to their limits and reverses the polarity of the equivalent modulating signal, see Fig. 16(a), so that the converter applies the switch positions that result in as fast a response as possible for the optimal amount of time. As for the torque step-up case, the MPC strategy fully utilizes the available dc-link voltage (see Fig. 16(b)) so that the settling time is only limited by the physical limits of the system. We conclude that the proposed direct MPC algorithm inherits the favorable dynamic behavior that characterizes direct control schemes. As for the PI-based FOC, it also tries to reverse the polarity of the modulating signal during the step-down scenario, but it does not manage to do it as aggressively as MPC, see Fig. 17(a). Moreover, during the step-up case, shown in Fig. 17(b), FOC tries to fully utilize the available dc-link voltage. In doing so, the modulating signal is saturated due to the employed anti-windup mechanism with saturation, but in a less aggressive manner due to the integrating element of the controller. Moreover, due to the fact that the controller (i.e., FOC) and modulator (i.e., SVM) are two decoupled entities that act independently from each other, the best possible dynamic performance is not guaranteed because the voltage synthesized by SVM is different from the voltage commanded by FOC [43]. As a result, the dynamics of FOC are slower, as also shown in Fig. 15.

Another scenario for evaluating the transient behavior of a controller is operation under speed changes. Since the focus of this work is on the inner current control loop designed in the framework of MPC, the load machine is used to impose a speed ramp of around $0.85\,$p.u., while keeping the current reference of the IM constant. As shown in Figs. 18 and 19, the MPC algorithm achieves good reference current tracking during these speed ramps.

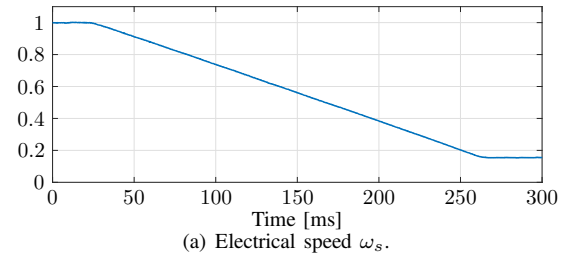

(a) Electrical speed ω_s.

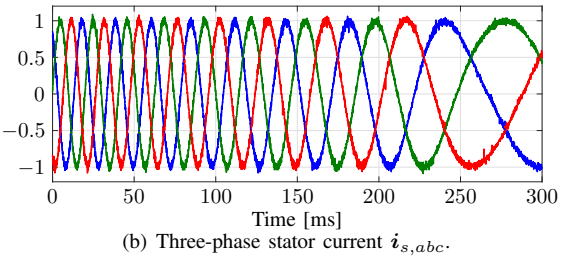

(b) Three-phase stator current $\boldsymbol{i}_{s,abc}$.

Fig. 18: Speed reference ramp (from 1 to 0.15 p.u.) with direct MPC.

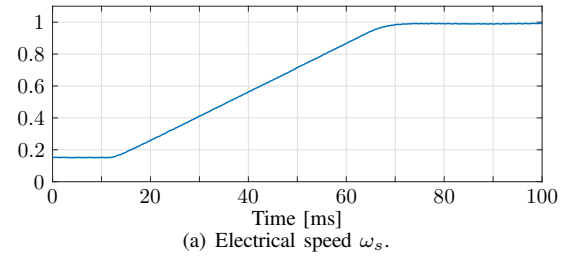

(a) Electrical speed ω_s.

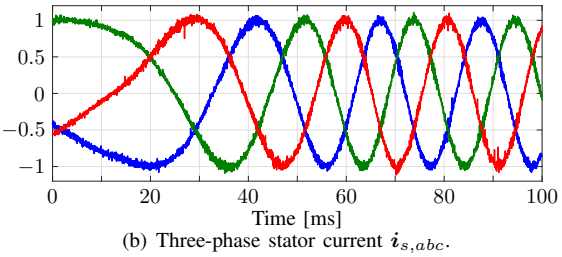

(b) Three-phase stator current $\boldsymbol{i}_{s,abc}$.

Fig. 19: Speed reference ramp (from 0.15 to 1 p.u.) with direct MPC.

C. Computational Burden

The main computational burden of the direct MPC scheme relates to the solution of the QP problem(s). Table IV summarizes the average and maximum number of iterations n_{it} required by the proposed QP algorithm to conclude to the optimal solution of one QP, along with the corresponding turnaround time $t_{\mathrm{ta,QP}}$ on dSPACE. In the same table, the turnaround time of the whole control scheme $t_{\mathrm{ta,tot}}$ is also shown. This time includes, besides the time required to solve the QP(s), the time needed for the analog-to-digital conversion (ADC), the uplink and downlink communication as well as the generation of the gating signals. As can be seen, the average number of iterations to solve one QP is 39.7 and the maximum 98. Considering that the optimization variable $\tilde{\boldsymbol{t}}$ of each QP problem is eight-dimensional, while eight boundary conditions exist along with two equality constrains, the required number of iterations is modest. Moreover, since each iteration of the proposed QP algorithm requires little computational effort, the

TABLE IV: Number of iterations required by the QP algorithm and the turnaround times on dSPACE, where $t_{\mathrm{ta,QP}}$ corresponds to solving one QP, and $t_{\mathrm{ta,tot}}$ to executing the whole control algorithm.

	Number of iterations n_{it}	Turnaround time $t_{\mathrm{ta,QP}}$ (µs)	Turnaround time $t_{\mathrm{ta,tot}}$ (µs)
Average	39.7	16.9	28.7
Maximum	98	42.6	71.3

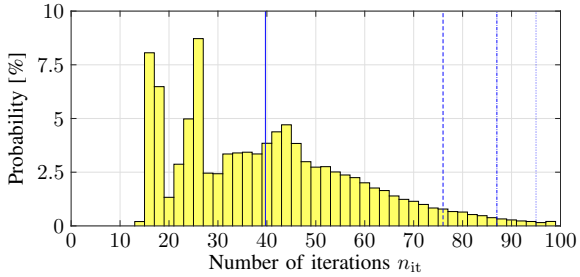

Fig. 20: Probability distribution of the number of iteration steps required by the QP algorithm. The average number of iterations is indicated by the solid vertical line. The 95, 98, and 99 percentiles are shown as dashed, dashed-dotted, and dotted vertical lines, respectively.

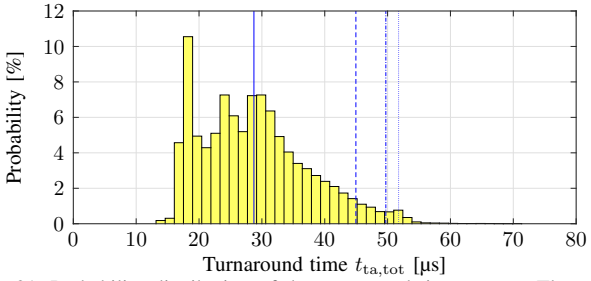

Fig. 21: Probability distribution of the turnaround time $t_{\mathrm{ta,tot}}$. The average turnaround time is indicated by the solid vertical line. The 95, 98, and 99 percentiles are shown as dashed, dashed-dotted, and dotted vertical lines, respectively.

TABLE V: The maximum turnaround time $t_{\mathrm{ta,max}}$ of the four discussed control algorithms running on dSPACE.

	FOC	FCS-MPC1	FCS-MPC2	Direct MPC
Turnaround time $t_{\mathrm{ta,max}}$ (µs)	16.6	16.9	17.1	71.3

maximum turnaround time of the proposed QP algorithm, i.e., $t_{\mathrm{ta,QP}}$, is as little as 42.6 µs. Furthermore, since the unsuited switching sequences can be effectively detected with only a few computations, the maximum turnaround time of the whole control scheme, i.e., $t_{\mathrm{ta,tot}}$, is only 71.3 µs. In addition, the probability distribution of the number of iterations n_{it} and the turnaround time $t_{\mathrm{ta,tot}}$ are shown in Figs. 20 and 21, respectively. As shown, in more than 98% cases, the turnaround time $t_{\mathrm{ta,tot}}$ is less than 50 µs. This indicates that the proposed QP solver manages to solve the necessary number of QPs in real time very quickly and within the available time, as defined by the chosen sampling interval of $T_s = 123.4$ µs, thanks the fast projection algorithm and the BB method discussed in Section IV.

Finally, the maximum (i.e., worst-case scenario) turnaround times $t_{\mathrm{ta,max}}$ of the four discussed control algorithms, i.e., the proposed direct MPC scheme, FOC, FCS-MPC1 and FCS-MPC2, are summarized in Table V. As can be seen, the superior performance of the proposed algorithm comes at a cost of increased computational demands. It is worth

mentioning, however, that, if needed, the turnaround time of the proposed control scheme can be significantly reduced, e.g., by decreasing the horizon to one step and/or by manipulating the maximum number of iteration steps, as can be deduced from Fig. 20. Nevertheless, such a reduction in the computational cost would occur at the expense of performance, i.e., a somewhat increased stator current THD.

VI. Conclusions

This paper proposed a computationally efficient QP solver that enabled the real-time implementation—and subsequent experimental evaluation—of the direct MPC scheme initially proposed in [24]. The proposed QP solver, by exploiting the specific feasible set of the QP problem underlying MPC, performs the projection onto it very quickly, which allows one to find the optimal solution with a relatively few number of iterations. Moreover, the proposed algorithm can exclude suboptimal solutions at a very early stage of the optimization process, thus greatly alleviating the associated computational effort.

In contrast to conventional FOC, the discussed direct MPC scheme directly manipulates the converter switch positions so that it can achieve short settling times during transients, on par with deadbeat control. However, thanks to the adopted control principles, and despite the absence of a modulator, the proposed direct MPC algorithm manages to achieve a constant switching frequency with a discrete harmonic spectrum. As a result, low current distortions are produced during steady-state operation. As shown for a two-level inverter driving an IM, the proposed direct MPC strategy achieves both lower current THD at steady-state operation and better dynamic behavior during transients than a conventional linear controller with a modulator, namely FOC with SVM.

Appendix

The vector $\boldsymbol{r}$ and matrix $\boldsymbol{M}$ in (13) are

$$\boldsymbol{r} = \begin{bmatrix} \boldsymbol{i}_{s,\mathrm{ref}}(t_0) - \boldsymbol{i}_s(t_0) \\ \boldsymbol{i}_{s,\mathrm{ref}}(t_0) - \boldsymbol{i}_s(t_0) \\ \boldsymbol{i}_{s,\mathrm{ref}}(t_0) - \boldsymbol{i}_s(t_0) \\ \Lambda(\boldsymbol{i}_{s,\mathrm{ref}}(T_s) - \boldsymbol{i}_s(t_0) - \boldsymbol{m}(t_3(k))T_s) \\ \boldsymbol{i}_{s,\mathrm{ref}}(T_s) - \boldsymbol{i}_s(t_0) \\ \boldsymbol{i}_{s,\mathrm{ref}}(T_s) - \boldsymbol{i}_s(t_0) \\ \boldsymbol{i}_{s,\mathrm{ref}}(T_s) - \boldsymbol{i}_s(t_0) \\ \Lambda(\boldsymbol{i}_{s,\mathrm{ref}}(2T_s) - \boldsymbol{i}_s(t_0) - \boldsymbol{m}(t_3(k+1))2T_s) \end{bmatrix}$$

and

$$\boldsymbol{M} = \begin{bmatrix} \boldsymbol{m}_{t_0} & \mathbf{0}_2 & \mathbf{0}_2 & \mathbf{0}_2 & \mathbf{0}_2 & \mathbf{0}_2 \\ \boldsymbol{m}_0 & \boldsymbol{m}_{t_1} & \mathbf{0}_2 & \mathbf{0}_2 & \mathbf{0}_2 & \mathbf{0}_2 \\ \boldsymbol{m}_0 & \boldsymbol{m}_1 & \boldsymbol{m}_{t_2} & \mathbf{0}_2 & \mathbf{0}_2 & \mathbf{0}_2 \\ \boldsymbol{\Lambda m}_0 & \boldsymbol{\Lambda m}_1 & \boldsymbol{\Lambda m}_2 & \mathbf{0}_2 & \mathbf{0}_2 & \mathbf{0}_2 \\ \boldsymbol{m}_0 & \boldsymbol{m}_1 & \boldsymbol{m}_2 & \boldsymbol{m}_{\bar{t}_0} & \mathbf{0}_2 & \mathbf{0}_2 \\ \boldsymbol{m}_0 & \boldsymbol{m}_1 & \boldsymbol{m}_2 & \boldsymbol{m}_{\bar{0}} & \boldsymbol{m}_{\bar{t}_1} & \mathbf{0}_2 \\ \boldsymbol{m}_0 & \boldsymbol{m}_1 & \boldsymbol{m}_2 & \boldsymbol{m}_{\bar{0}} & \boldsymbol{m}_{\bar{1}} & \boldsymbol{m}_{\bar{t}_2} \\ \boldsymbol{\Lambda m}_0 & \boldsymbol{\Lambda m}_1 & \boldsymbol{\Lambda m}_2 & \boldsymbol{\Lambda m}_{\bar{0}} & \boldsymbol{\Lambda m}_{\bar{1}} & \boldsymbol{\Lambda m}_{\bar{2}} \end{bmatrix}$$

with

$$\begin{aligned} \boldsymbol{m}_{t_i} &= \boldsymbol{m}(t_i(k)) - \boldsymbol{m}_{\mathrm{ref}}(k) \\ \boldsymbol{m}_{\bar{t}_i} &= \boldsymbol{m}(t_i(k+1)) - \boldsymbol{m}_{\mathrm{ref}}(k+1) \\ \boldsymbol{m}_i &= \boldsymbol{m}(t_i(k)) - \boldsymbol{m}(t_{i+1}(k)) \\ \boldsymbol{m}_{\bar{i}} &= \boldsymbol{m}(t_i(k+1)) - \boldsymbol{m}(t_{i+1}(k+1)) \end{aligned}$$

where $i \in \{0,\ 1,\ 2\}$ and $t_0(k+1) = T_s$.

The vector $\tilde{\boldsymbol{r}}$ and matrix $\tilde{\boldsymbol{M}}$ in (20) are

$$\tilde{\boldsymbol{r}} = \begin{bmatrix} \boldsymbol{i}_{s,\mathrm{ref}}(t_0) - \boldsymbol{i}_s(t_0) \\ \boldsymbol{i}_{s,\mathrm{ref}}(t_0) - \boldsymbol{i}_s(t_0) \\ \boldsymbol{i}_{s,\mathrm{ref}}(t_0) - \boldsymbol{i}_s(t_0) \\ \boldsymbol{\Lambda}(\boldsymbol{i}_{s,\mathrm{ref}}(t_0) - \boldsymbol{i}_s(t_0)) \\ \boldsymbol{i}_{s,\mathrm{ref}}(t_0) - \boldsymbol{i}_s(t_0) \\ \boldsymbol{i}_{s,\mathrm{ref}}(t_0) - \boldsymbol{i}_s(t_0) \\ \boldsymbol{i}_{s,\mathrm{ref}}(t_0) - \boldsymbol{i}_s(t_0) \\ \boldsymbol{\Lambda}(\boldsymbol{i}_{s,\mathrm{ref}}(t_0) - \boldsymbol{i}_s(t_0)) \end{bmatrix}$$

and

$$\tilde{\boldsymbol{M}} = \begin{bmatrix} \tilde{\boldsymbol{m}}_0 & \mathbf{0}_2 & \mathbf{0}_2 & \mathbf{0}_2 & \mathbf{0}_2 & \mathbf{0}_2 & \mathbf{0}_2 & \mathbf{0}_2 \\ \tilde{\boldsymbol{m}}_0 & \tilde{\boldsymbol{m}}_1 & \mathbf{0}_2 & \mathbf{0}_2 & \mathbf{0}_2 & \mathbf{0}_2 & \mathbf{0}_2 & \mathbf{0}_2 \\ \tilde{\boldsymbol{m}}_0 & \tilde{\boldsymbol{m}}_1 & \tilde{\boldsymbol{m}}_2 & \mathbf{0}_2 & \mathbf{0}_2 & \mathbf{0}_2 & \mathbf{0}_2 & \mathbf{0}_2 \\ \tilde{\boldsymbol{m}}_{0\boldsymbol{\Lambda}} & \tilde{\boldsymbol{m}}_{1\boldsymbol{\Lambda}} & \tilde{\boldsymbol{m}}_{2\boldsymbol{\Lambda}} & \tilde{\boldsymbol{m}}_{3\boldsymbol{\Lambda}} & \mathbf{0}_2 & \mathbf{0}_2 & \mathbf{0}_2 & \mathbf{0}_2 \\ \tilde{\boldsymbol{m}}_0 & \tilde{\boldsymbol{m}}_1 & \tilde{\boldsymbol{m}}_2 & \tilde{\boldsymbol{m}}_3 & \tilde{\boldsymbol{m}}_0 & \mathbf{0}_2 & \mathbf{0}_2 & \mathbf{0}_2 \\ \tilde{\boldsymbol{m}}_0 & \tilde{\boldsymbol{m}}_1 & \tilde{\boldsymbol{m}}_2 & \tilde{\boldsymbol{m}}_3 & \tilde{\boldsymbol{m}}_{\bar{0}} & \tilde{\boldsymbol{m}}_{\bar{1}} & \mathbf{0}_2 & \mathbf{0}_2 \\ \tilde{\boldsymbol{m}}_0 & \tilde{\boldsymbol{m}}_1 & \tilde{\boldsymbol{m}}_2 & \tilde{\boldsymbol{m}}_3 & \tilde{\boldsymbol{m}}_{\bar{0}} & \tilde{\boldsymbol{m}}_{\bar{1}} & \tilde{\boldsymbol{m}}_{\bar{2}} & \mathbf{0}_2 \\ \tilde{\boldsymbol{m}}_{0\boldsymbol{\Lambda}} & \tilde{\boldsymbol{m}}_{1\boldsymbol{\Lambda}} & \tilde{\boldsymbol{m}}_{2\boldsymbol{\Lambda}} & \tilde{\boldsymbol{m}}_{3\boldsymbol{\Lambda}} & \tilde{\boldsymbol{m}}_{\bar{0}\boldsymbol{\Lambda}} & \tilde{\boldsymbol{m}}_{\bar{1}\boldsymbol{\Lambda}} & \tilde{\boldsymbol{m}}_{\bar{2}\boldsymbol{\Lambda}} & \tilde{\boldsymbol{m}}_{\bar{3}\boldsymbol{\Lambda}} \end{bmatrix}$$

with

$$\begin{aligned} \tilde{\boldsymbol{m}}_i &= \boldsymbol{m}(t_i(k)) - \boldsymbol{m}_{\mathrm{ref}}(k)) \\ \tilde{\boldsymbol{m}}_{i\boldsymbol{\Lambda}} &= \boldsymbol{\Lambda}\tilde{\boldsymbol{m}}_i \\ \tilde{\boldsymbol{m}}_{\bar{i}} &= \boldsymbol{m}(t_i(k+1)) - \boldsymbol{m}_{\mathrm{ref}}(k+1)) \\ \tilde{\boldsymbol{m}}_{\bar{i}\boldsymbol{\Lambda}} &= \boldsymbol{\Lambda}\tilde{\boldsymbol{m}}_{\bar{i}} \end{aligned}$$

where $i \in \{0, 1, 2, 3\}$.

The matrix $\boldsymbol{T}$ in (23) is

$$\boldsymbol{T} = \begin{bmatrix} \tilde{\boldsymbol{I}} & \mathbf{0}_3 & \mathbf{0}_{3\times 3} & \mathbf{0}_3 \\ \mathbf{0}_{3\times 3} & \mathbf{0}_3 & \tilde{\boldsymbol{I}} & \mathbf{0}_3 \end{bmatrix},$$

where $\tilde{\boldsymbol{I}}$ is

$$\tilde{\boldsymbol{I}} = \begin{bmatrix} 1 & 0 & 0 \\ 1 & 1 & 0 \\ 1 & 1 & 1 \end{bmatrix}.$$

References

[1] P. Cortés, M. P. Kazmierkowski, R. M. Kennel, D. E. Quevedo, and J. Rodríguez, "Predictive control in power electronics and drives," *IEEE Trans. Ind. Electron.*, vol. 55, no. 12, pp. 4312–4324, Dec. 2008.

[2] P. Karamanakos, E. Liegmann, T. Geyer, and R. Kennel, "Model predictive control of power electronic systems: Methods, results, and challenges," *IEEE Open J. Ind. Appl.*, vol. 1, pp. 95–114, 2020.

[3] T. Geyer, *Model predictive control of high power converters and industrial drives*. Hoboken, NJ, USA: Wiley, 2016.

[4] P. Karamanakos and T. Geyer, "Guidelines for the design of finite control set model predictive controllers," *IEEE Trans. Power Electron.*, vol. 35, no. 7, pp. 7434–7450, Jul. 2020.

[5] T. Geyer, "A comparison of control and modulation schemes for medium-voltage drives: Emerging predictive control concepts versus PWM-based schemes," *IEEE Trans. Ind. Appl.*, vol. 47, no. 3, pp. 1380–1389, May/Jun. 2011.

[6] P. Cortes, J. Rodriguez, D. E. Quevedo, and C. Silva, "Predictive current control strategy with imposed load current spectrum," *IEEE Trans. Power Electron.*, vol. 23, no. 2, pp. 612–618, Mar. 2008.

[7] A. Bouafia, J. Gaubert, and F. Krim, "Predictive direct power control of three-phase pulsewidth modulation (PWM) rectifier using space-vector modulation (SVM)," *IEEE Trans. Power Electron.*, vol. 25, no. 1, pp. 228–236, Jan. 2010.

[8] R. O. Ramírez, J. R. Espinoza, F. Villarroel, E. Maurelia, and M. E. Reyes, "A novel hybrid finite control set model predictive control scheme with reduced switching," *IEEE Trans. Ind. Electron.*, vol. 61, no. 11, pp. 5912–5920, Nov. 2014.

[9] M. Pacas and J. Weber, "Predictive direct torque control for the PM synchronous machine," *IEEE Trans. Ind. Electron.*, vol. 52, no. 5, pp. 1350–1356, Oct. 2005.

[10] P. Karamanakos, P. Stolze, R. M. Kennel, S. Manias, and H. du Toit Mouton, "Variable switching point predictive torque control of induction machines," *IEEE J. Emerg. Sel. Topics Power Electron.*, vol. 2, no. 2, pp. 285–295, Jun. 2014.

[11] Y. Zhang, W. Xie, Z. Li, and Y. Zhang, "Low-complexity model predictive power control: Double-vector-based approach," *IEEE Trans. Ind. Electron.*, vol. 61, no. 11, pp. 5871–5880, Nov. 2014.

[12] L. Tarisciotti, P. Zanchetta, A. Watson, J. C. Clare, M. Degano, and S. Bifaretti, "Modulated model predictive control for a three-phase active rectifier," *IEEE Trans. Ind. Appl.*, vol. 51, no. 2, pp. 1610–1620, Mar./Apr. 2015.

[13] Q. Liu and K. Hameyer, "Torque ripple minimization for direct torque control of PMSM with modified FCSMPC," *IEEE Trans. Ind. Appl.*, vol. 52, no. 6, pp. 4855–4864, Nov./Dec. 2016.

[14] M. Tomlinson, H. d. T. Mouton, R. Kennel, and P. Stolze, "A fixed switching frequency scheme for finite-control-set model predictive control—concept and algorithm," *IEEE Trans. Ind. Electron.*, vol. 63, no. 12, pp. 7662–7670, Dec. 2016.

[15] P. Karamanakos, A. Ayad, and R. Kennel, "A variable switching point predictive current control strategy for quasi-Z-source inverters," *IEEE Trans. Ind. Appl.*, vol. 54, no. 2, pp. 1469–1480, Mar./Apr. 2018.

[16] Y. Zhang, Y. Bai, and H. Yang, "A universal multiple-vector-based model predictive control of induction motor drives," *IEEE Trans. Power Electron.*, vol. 33, no. 8, pp. 6957–6969, Aug. 2018.

[17] C. Zheng, T. Dragičević, B. Majmunović, and F. Blaabjerg, "Constrained modulated-model predictive control of an LC-filtered voltage source converter," *IEEE Trans. Power Electron.*, vol. 35, no. 2, pp. 1967–1977, Feb. 2020.

[18] L. Tarisciotti, A. Formentini, A. Gaeta, M. Degano, P. Zanchetta, R. Rabbeni, and M. Pucci, "Model predictive control for shunt active filters with fixed switching frequency," *IEEE Trans. Ind. Appl.*, vol. 53, no. 1, pp. 296–304, Jan./Feb. 2017.

[19] S. A. Larrinaga, M. A. R. Vidal, E. Oyarbide, and J. R. T. Apraiz, "Predictive control strategy for dc/ac converters based on direct power control," *IEEE Trans. Ind. Electron.*, vol. 54, no. 3, pp. 1261–1271, Jun. 2007.

[20] S. Vazquez, A. Marquez, R. Aguilera, D. Quevedo, J. I. Leon, and L. G. Franquelo, "Predictive optimal switching sequence direct power control for grid-connected power converters," *IEEE Trans. Ind. Electron.*, vol. 62, no. 4, pp. 2010–2020, Apr. 2015.

[21] A. Mora, R. Cárdenas-Dobson, R. P. Aguilera, A. Angulo, F. Donoso, and J. Rodríguez, "Computationally efficient cascaded optimal switching sequence MPC for grid-connected three-level NPC converters," *IEEE Trans. Power Electron.*, vol. 34, no. 12, pp. 12 464–12 475, Dec. 2019.

[22] S. Vazquez, P. Acuña, R. P. Aguilera, J. Pou, J. I. Leon, and L. G. Franquelo, "Dc-link voltage balancing strategy based on optimal switching sequences model predictive control for single-phase H-NPC converters," *IEEE Trans. Ind. Electron.*, vol. 67, no. 9, pp. 7410–7420, Sep. 2020.

[23] W. Falmbigl, S. Jakubek, O. König, and G. Prochart, "Predictive pulse pattern control for a synchronous multiphase buck converter," in *Proc. IEEE Int. Symp. Pred. Control of Elect. Drives and Power Electron.*, Pilsen, Czech Republich, Sep. 2017, pp. 60–65.

[24] P. Karamanakos, R. Mattila, and T. Geyer, "Fixed switching frequency direct model predictive control based on output current gradients," in *Proc. IEEE Ind. Electron. Conf.*, Washington, D.C., USA, Oct. 2018, pp. 2329–2334.

[25] D. G. Holmes and T. A. Lipo, *Pulse Width Modulation for Power Converters: Principles and Practice*. Piscataway, NJ: IEEE Press, 2003.

[26] D. Kouzoupis, A. Zanelli, H. Peyrl, and H. J. Ferreau, "Towards proper assessment of QP algorithms for embedded model predictive control," in *Proc. of the Eur. Control Conf.*, Linz, Austria, Jul. 2015, pp. 2609–2616.

[27] J. Holtz, "The representation of ac machine dynamics by complex signal flow graphs," *IEEE Trans. Ind. Electron.*, vol. 42, no. 3, pp. 263–271, Jun. 1995.

[28] P. Karamanakos, M. Nahalparvari, and T. Geyer, "Fixed switching frequency direct model predictive control with continuous and discontinuous modulation for grid-tied converters with LCL filters," *IEEE Trans. Control Syst. Technol.*, vol. 29, no. 4, pp. 1503–1518, 2021.

[29] T. Geyer, P. Karamanakos, and R. Kennel, "On the benefit of long-horizon direct model predictive control for drives with LC filters," in *Proc. IEEE Energy Convers. Congr. Expo.*, Pittsburgh, PA, USA, Sep. 2014, pp. 3520–3527.

[30] T. Geyer, "Algebraic tuning guidelines for model predictive torque and flux control," *IEEE Trans. Ind. Appl.*, vol. 54, no. 5, pp. 4464–4475, Sep./Oct. 2018.

[31] A. G. Beccuti, S. Mariéthoz, S. Cliquennois, S. Wang, and M. Morari, "Explicit model predictive control of dc-dc switched-mode power supplies with extended Kalman filtering," *IEEE Trans. Ind. Electron.*, vol. 56, no. 6, pp. 1864–1874, Jun. 2009.

[32] J. Rodas, F. Barrero, M. R. Arahal, C. Martín, and R. Gregor, "Online estimation of rotor variables in predictive current controllers: A case study using five-phase induction machines," *IEEE Trans. Ind. Electron.*, vol. 63, no. 9, pp. 5348–5356, Sep. 2016.

[33] D. J. Atkinson, P. P. Acarnley, and J. W. Finch, "Observers for induction motor state and parameter estimation," *IEEE Trans. Ind. Appl.*, vol. 27, no. 6, pp. 1119–1127, Dec. 1991.

[34] J. Nocedal and S. Wright, *Numerical optimization*, 2nd ed. New York, NY, USA: Springer, 2006.

[35] S. Richter, T. Geyer, and M. Morari, "Resource-efficient gradient methods for model predictive pulse pattern control on an FPGA," *IEEE Trans. Control Syst. Technol.*, vol. 25, no. 3, pp. 828–841, May 2017.

[36] A. B. Németh and S. Z. Németh, "How to project onto an isotone projection cone," *Linear Algebra Appl.*, vol. 433, no. 1, pp. 41–51, Jul. 2010.

[37] S. Boyd and L. Vandenberghe, *Convex Optimization*. Cambridge, UK: Cambridge Univ. Press, 2004.

[38] J. Barzilai and J. M. Borwein, "Two-point step size gradient methods," *IMA J. of Num. Anal.*, vol. 8, no. 1, pp. 141–148, Jan. 1988.

[39] Y.-H. Dai and R. Fletcher, "New algorithms for singly linearly constrained quadratic programs subject to lower and upper bounds," *Math. Program.*, vol. 106, no. 3, pp. 403–421, May 2006.

[40] R. Fletcher, "On the Barzilai-Borwein method," in *Optim. and Control with Appl.* Boston, MA, USA: Springer, 2005, pp. 235–256.

[41] Y.-H. Dai and R. Fletcher, "Projected Barzilai-Borwein methods for large-scale box-constrained quadratic programming," *Numer. Math.*, vol. 100, no. 1, pp. 21–47, Mar. 2005.

[42] G. M. Joksimović, J. Riger, T. M. Wolbank, N. Perić, and M. Vašak, "Stator-current spectrum signature of healthy cage rotor induction machines," *IEEE Trans. Ind. Electron.*, vol. 60, no. 9, pp. 4025–4033, Sep. 2013.

[43] J.-K. Seok, J.-S. Kim, and S.-K. Sul, "Overmodulation strategy for high-performance torque control," *IEEE Trans. Power Electron.*, vol. 13, no. 4, pp. 786–792, Jul. 1998.

Qifan Yang was born in Anhui, China, in 1995. He received the B.Eng. degree in electrical engineering Xi'an Jiaotong University, Xi'an, Shannxi, China, in 2016, and the M.Sc. degree in electrical power engineering from Technical University of Munich, Munich, Germany, in 2019. Since 2019, he has been pursuing the Ph.D. degree at the Chair of Electrical Drive Systems and Power Electronics, Technical University of Munich (TUM), Germany. His research interest include optimal control, power electronics and electrical drives.

Petros Karamanakos (S'10 – M'14 – SM'19) received the Diploma and Ph.D. degrees in electrical and computer engineering from the National Technical University of Athens (NTUA), Athens, Greece, in 2007, and 2013, respectively.

From 2010 to 2011 he was with the ABB Corporate Research Center, Baden-Dättwil, Switzerland, where he worked on model predictive control strategies for medium-voltage drives. From 2013 to 2016 he was a PostDoc Research Associate in the Chair of Electrical Drive Systems and Power Electronics, Technische Universität München, Munich, Germany. Since September 2016, he has been an Assistant Professor in the Faculty of Information Technology and Communication Sciences, Tampere University, Tampere, Finland. His main research interests lie at the intersection of optimal control, mathematical programming and power electronics, including model predictive control and optimal modulation for power electronic converters and ac variable speed drives.

Dr. Karamanakos received the 2014 Third Best Paper Award of the IEEE Transactions on Industry Applications and two Prize Paper Awards at conferences. He serves as an Associate Editor of the IEEE Transactions on Industry Applications and of the IEEE Open Journal of Industry Applications.

Wei Tian was born in Taizhou, Jiangsu, China, in 1989. He received the B.Eng. degree in electrical engineering and automation from Central South University (CSU), Changsha, China, in 2012 and the M.Sc. degree in electrical power engineering from RWTH Aachen University, Aachen, Germany, in 2015. Since 2016, he has been pursuing the Ph.D. degree at the Chair of Electrical Drive Systems and Power Electronics, Technical University of Munich (TUM), Munich, Germany. His research interests include power electronics and electrical drives, model predictive control, and modular multilevel converter.

Xiaonan Gao (S'18-M'21) was born in Liaoning, China, in 1990. He received the B.S. and M.S. degrees in electrical engineering from the Dalian University of Technology, Dalian, China, in 2013 and 2016, respectively.

He is currently working toward the Ph.D. degree with the Institute for Electrical Drive Systems and Power Electronics, Technical University of Munich, Germany. His research interests include power electronics and electrical drives, predictive control, and multilevel converters.

Xinyue Li was born in Yunnan, China, in 1991. She received her B.S. degree in electrical engineering from Tsinghua University, Beijing, China, in 2013, and the M.S. degree in electrical engineering, information technology and computer engineering from the RWTH Aachen University, Aachen, Germany, in 2017. She is currently working toward the Dr. Ing (Ph.D.) degree with the Institute for Electrical Drive Systems and Power Electronics, Technical University of Munich, Munich, Germany.

Since 2017, she has been with the research and Development Department, Bosch Rexroth AG, Germany. Her research interests include parameter identification, robust and optimal control of ac machines.

Tobias Geyer (M'08 – SM'10) received the Dipl.-Ing. and Ph.D. degrees in electrical engineering from ETH Zurich, Zurich, Switzerland, in 2000 and 2005, respectively, and the Habilitation degree in power electronics from ETH Zurich, Zurich, Switzerland, in 2017.

After his Ph.D., he spent three years at GE Global Research, Munich, Germany, three years at the University of Auckland, Auckland, New Zealand, and eight years at ABB's Corporate Research Centre, Baden-Dättwil, Switzerland. There, in 2016, he became a Senior Principal Scientist for power conversion control. He was appointed as an extraordinary Professor at Stellenbosch University, Stellenbosch, South Africa, from 2017 to 2023. In 2020, he joined ABB's medium-voltage drives business as R&D platform manager of the ACS6080.

He is the author of 35 patent families and the book "Model predictive control of high power converters and industrial drives" (Wiley, 2016). He teaches a regular course on model predictive control at ETH Zurich. His research interests include medium-voltage and low-voltage drives, utility-scale power converters, optimized pulse patterns and model predictive control.

Dr. Geyer received the Semikron Innovation Award and the Nagamori Award, both in 2021. He is also the recipient of the 2017 First Place Prize Paper Award in the Transactions on Power Electronics, the 2014 Third Place Prize Paper Award in the Transactions on Industry Applications, and of two Prize Paper Awards at conferences. He is a former Associate Editor for the Transactions on Industry Applications (from 2011 until 2014) and the Transactions on Power Electronics (from 2013 until 2019). He was an international program committee vice chair of the IFAC conference on Nonlinear Model Predictive Control in Madison, WI, USA, in 2018. Dr. Geyer is a Distinguished Lecturer of the Power Electronics Society in the years 2020 and 2021.

Ralph Kennel (M'89-SM'96) was born in Kaiserslautern, Germany, in 1955. He received the Diploma and Dr. Ing. (Ph.D.) degrees in electrical engineering from the University of Kaiserslautern, Kaiserslautern, Germany, in 1979 and 1984, respectively.

From 1983 to 1999, he worked on several positions with Robert BOSCH GmbH (Germany). Until 1997, he was responsible for the development of servo drives. From 1994 to 1999, he was a Visiting Professor with the University of Newcastle-upon-Tyne, Newcastle-upon-Tyne, U.K. From 1999 to 2008, he was a Professor of electrical machines and drives with Wuppertal University, Wuppertal, Germany. Since 2008, he has been a Professor of electrical drive systems and power electronics with Technical University of Munich, Munich, Germany. His current main interests include renewable energy systems, sensorless control of ac drives, predictive control of power electronics, and hardware-in-the-loop systems.

Dr. Kennel is a Fellow of the IEE and a Chartered Engineer in the U.K. within IEEE, he is a Treasurer of the Germany Section as well as ECCE Global Partnership Chair of the Power Electronics society. He is an Associate Editor for the IEEE TRANSACTIONS ON POWER ELECTRONICS.